Superconductor Science and Technology

Stress and strain analysis of a REBCO high field coil based on the distribution of shielding current

Stress and strain analysis of a REBCO high field coil based on the distribution of shielding current

Jing Xia[1,*], Hongyu Bai[2], Huadong Yong[3], Hubertus W Weijers[2], Thomas A Painter[2], Mark D Bird[2]

[1] Institute of Applied Physics and Computational Mathematics, Beijing 100094, People's Republic of China

[2] National High Magnetic Field Laboratory, Florida State University, Tallahassee, FL 32310, USA

[3] Department of Mechanics and Engineering Sciences, College of Civil Engineering and Mechanics, Lanzhou University, Lanzhou, Gansu 730000, People's Republic of China

*This work was originally started when Jing Xia worked at the National High Magnetic Field Laboratory, Tallahassee, and was subsequently finished at the Institute of Applied Physics and Computational Mathematics, Beijing.

E-mail: power_xj@163.com

Abstract There are growing concerns about the stresses created by shielding currents in high field superconducting magnets fabricated from tape conductors leading to reduced performance and lifetime. This paper presents results of stress/strain calculations caused by shielding currents assuming the conductor deformations are linear. An anisotropic bulk approximation approach was used to calculate the electromagnetic field distributions in a REBCO high field coil with a stack of pancakes and a large number of turns first, and then the Lorentz force distribution and mechanical response characteristics were studied in the two-dimensional axisymmetric configuration. A new discrete contact mechanical model implemented by the finite element method, which is able to simulate the contact and separation behaviors between adjacent turns during the deformation, was proposed to analyze the distributions of hoop stress, hoop strain, radial stress and radial displacement in the coil. The influences of shielding current on those mechanical responses were obtained by comparing the simulation cases with and without taking shielding current into account. Besides, a continuum bulk mechanical model, which is parallel to the discrete contact mechanical model and treats the pancakes as continuum bulks, was modeled as well in order to understand the influences of different models on the simulation results. Furthermore, we studied the influences of a couple of practical factors (including the n-value, ramp rate, and operating mode of the REBCO coil winding) on the shielding current and hoop stress.

A couple of novel and important conclusions were found. 1) Neglecting the shielding current behavior would significantly underestimate the maximum local hoop stress in a REBCO high field coil. 2) The continuum bulk mechanical model is not adequate for the stress analysis of dry-wound high field coils, by which unreasonably large tensile radial stresses could be obtained. 3) The highest local hoop stresses at the fully-charged moment and the fully-discharged moment are located in a certain pancake near the end of the coil winding and the end pancake, respectively. 4) Decreasing the n-value and the ramp rate of the REBCO coil could be two auxiliary ways to suppress the shielding current and maximum local hoop stress in the coil. 5) For the ramp-and-hold operating mode, the REBCO coil experiences the highest stress level at the moment when it right achieves the goal field. 6) The cycling operation of a REBCO high field coil can cause the tape experiencing alternative positive and negative stresses and this may decrease the fatigue life of the tape and then the life of a magnet.

Keywords REBCO high field coil, REBCO pancake coil, shielding current, hoop stress, mechanical response, Lorentz force

1. Introduction

Strain sensitivity of coil performance is a very significant and general problem in the history of developing superconducting magnet technologies. The mechanical characteristics in low-temperature superconducting (LTS) cable-in-conduit conductors (CICCs) have been widely studied and debated over the past decades [1-5]. Compared to CICC strands, high-temperature superconductors (HTSs), especially REBCO coated conductors, demonstrate much lower strain sensitivity with respect to the current transport property and intrinsic higher tensile tolerance exceeding $600\ \mathrm{MPa}$. The excellent critical current performance under high magnetic field and the strong mechanical property prompt researchers to pursue more powerful superconducting magnets with compact constructions by winding REBCO tapes into pancake coils or layer-wound solenoids [6]. A new record all-superconducting user magnet, constructed at the National High Magnetic Field Laboratory (NHMFL), reached its full field of $32\ \mathrm{T}$ at the end of 2017, and an early exploration for developing the next-generation of high field superconducting magnets towards 40 T was launched recently [7]. Under such high magnetic field condition associated with large operating current densities in the coil windings, there are more and more concerns about the mechanical issues. For one thing, high hoop stress can lead to a severe degeneration of the critical current after the irreversible strain limit is exceeded. Besides, it was reported that high hoop stress could bring out large stress concentration in the soldered joint, inducing the cleavage and peeling of the conductor there [8]. Therefore, it is important to obtain a deep understanding on the characteristics of stress/strain distributions in REBCO high field coils.

There are two kinds of mainstream approaches to analyze the stress/strain distributions in REBCO coils currently. The most widely used is an analytic formula in the form of the product of the radius, current density and magnetic field, which gives a very simple way to roughly estimate the hoop stresses in a coil [9]. The other approach originates from [10], in which Gray and Ballou neglected the axial dimension of the coil and used the classic elastic theory with plane stress state to analytically solve the stress, strain, and displacement in the coil, where the coil was treated as a plane disk and a transversely isotropic constitutive relation in the plane stress state was adopted. Following [10], a few specific calculations were performed for Bi-2223 and REBCO pancake coils and some strain measures were carried out for comparison [11-14]. Note that the classic plane disk model is a continuum model, which cannot take into account the separation behavior of adjacent turns in a coil. Recently, based on the aforementioned classic model, Wang *et al* [15, 16] developed a combined homogeneous cylinder model to study the effects of the winding tension and overband over the outer radius of a pancake on the mechanical behaviors. Their theoretical results showed that suitable winding tension and overbanding condition could effectively reduce the maximum hoop stress in the REBCO coil. More recently, Liu *et al* [17] studied the mechanical responses in a no-insulation REBCO layer-wound coil after quench, based on a thermal-coupled electromagnetic model and a two-dimensional axisymmetric bulk mechanical model.

However, all the aforementioned methods did not consider the shielding current induced in winding turns, which is an intrinsic electromagnetic behavior existing in superconducting tapes to resist the magnetic field from penetrating into themselves. Namely, in the previous studies, the current density distribution in each turn was uniform and the influence of shielding current on the magnetic field distribution also could not be taken into account, which resulted in a significant deviation on determining the Lorentz force distribution in the coil. In fact, a pair of azimuthal currents with opposite directions flow in each winding turn [18-20], which will bring out a considerable effect of radial shear on the deformation of the pancake in a high axial magnetic field condition. Therefore, nonuniform radial deformation will appear in the height direction of the pancake and rather high local hoop stress may be generated in the turns.

In this paper, the two-dimensional axisymmetric configuration with respect to the cross section of a coil winding will be adopted to study the mechanical responses in a REBCO high field coil with a stack of pancakes and a large number of turns, on a basis of a calculation result of the shielding current distribution. Two mechanical models in association with a transversely isotropic constitutive relation in three-dimensional stress state are proposed to calculate the distributions of stress, strain and displacement in the coil. In section 2, the electromagnetic model for calculating the electromagnetic field distributions with taking shielding current into account is introduced first. Subsequently, the two mechanical models, i.e., the continuum bulk model and the discrete contact model, are introduced in detail. In section 3, the distributions of electromagnetic field, Lorentz force, stress, strain and displacement in the coil are given. The influences of shielding current on the mechanical responses are discussed and the effect of employing different mechanical models on determining the simulation results is presented. In section 4, we further study the influences of a couple of practical factors on the shielding current and hoop stress. In section 5, we summarize the conclusions.

2. Model descriptions

The full-size 20/70 coil of the dual-coil HTS insert in the NHMFL 32 T all-superconducting magnet [21, 22] is chosen as a specific example for the stress/strain analysis, accompanying with the LTS outer magnet which plays the role on providing a 15 T background field. The analysis results of the full-size HTS insert with dual coils are not presented here because using a single coil winding is more convenient and straightforward to give an insight into the general mechanical response characteristics of REBCO high field coils. The 20/70 HTS coil consists of 20 double pancakes which are co-wound with one turn of un-insulated REBCO tape and one turn of insulated stainless steel (SS) tape. The LTS multisection outer magnet with a combination of three Nb_3Sn coil windings and two NbTi coil windings in reality [22] is simplified as two concentric coil windings here. The coil system depicted is illustrated in figure 1 and the design parameters are listed in table 1.

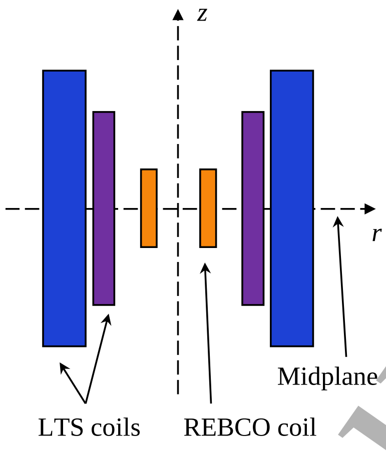

Figure 1. Schematic drawing of the superconducting coil system.

Table 1. Design parameters of the high field coil system.

Coil	Parameter	Value
REBCO coil	Inner/outer radii (mm)	20/70
	Number of pancakes	40
	Turns per pancake	244
	Tape width (mm)	4
	Insulation gap between adjacent pancakes (mm)	0.45
	Height of coil (mm)	177.55
	Coil current density (A/mm^2)	197
	Field contribution (T)	10.7
LTS coil I	Inner/outer radii (mm)	135/190
	Height of coil (mm)	500
	Coil current density (A/mm^2)	130
LTS coil II	Inner/outer radii (mm)	214/310
	Height of coil (mm)	620
	Coil current density (A/mm^2)	81
	Total field contribution of LTS coils (T)	15

2.1. Electromagnetic model

The REBCO conductor/insulated SS co-wound pancake coil will be simplified as a series of concentric independent cylindrical layers, and thus can be dealt with in the way of two-dimensional axisymmetric problem. An anisotropic bulk model formulated in the form of two-dimensional axisymmetric *H*-formulation was developed successfully to simulate the time-dependent electromagnetic behaviors of high field REBCO pancake coils in our previous work [18]. Now a brief introduction to the anisotropic bulk model is presented as follows and more details are available in [18].

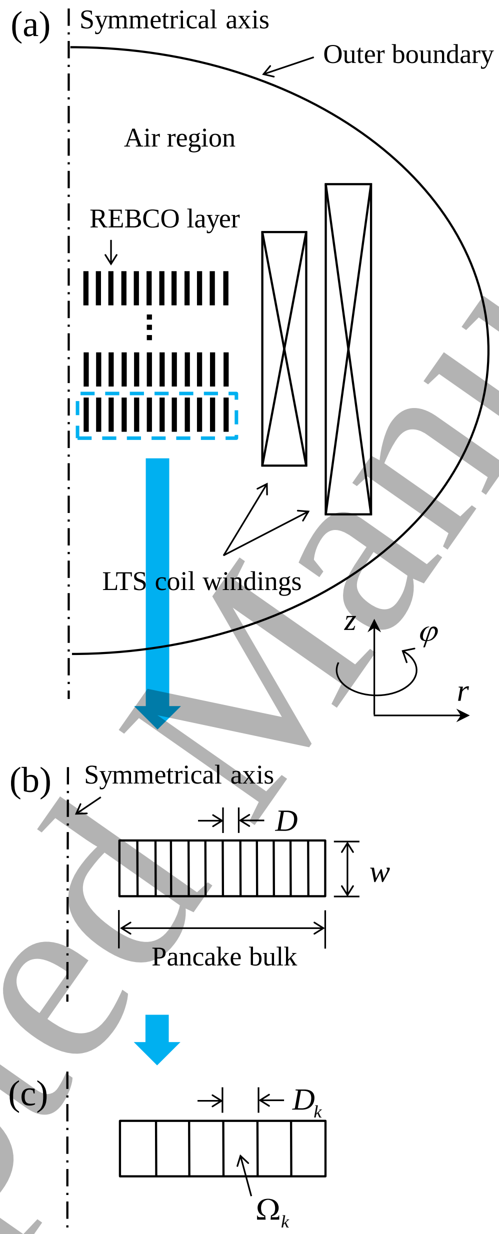

Figure 2. Schematic drawing of the two-dimensional axisymmetric electromagnetic model.

Figure 2(a) gives the schematic drawing of the two-dimensional axisymmetric model. The solving region consists of the REBCO layers in the pancakes, the LTS coil windings and the air surrounding them. Considering the symmetry of flux distribution with respect to the midplane of the coil windings, only half of the full-size construction is needed to solve once we constrain the radial magnetic field component equal to be zero on the boundary of midplane. The power law is used to describe the $E-J$ constitutive relation for the HTS region and the corresponding effective resistivity ρ has a form of

$$\rho = E_0 \left| \frac{J_\varphi}{J_c(B,\theta)} \right|^{n-1} \frac{1}{J_c(B,\theta)}, \tag{1}$$

where J_φ, E_0 and n are the current density in the azimuthal direction, the voltage criterion for the critical current density, and the flux creep exponent, respectively. $E_0 = 1\times10^{-4}$ V m^{-1} is used throughout in this paper and n is specified as 25 unless otherwise stated. The critical current density J_c in the REBCO layer has an essential anisotropic property with respect to the magnetic field. A practical fit function for the corresponding critical current $I_c(B,\theta)$ is employed here [23]:

$$\begin{aligned} I_c(B,\theta) &= \frac{k_0}{(B+\beta_0)^{\alpha_0}} + \frac{k_1}{(B+\beta_1)^{\alpha_1}} \times \left[\omega_1^2(B)\cos^2(\theta-\varphi_1) + \sin^2(\theta-\varphi_1) \right]^{-1/2}, \\ \omega_1(B) &= c_1 \left[B + \left(\frac{1}{c_1} \right)^{1/\varepsilon_1} \right]^{\varepsilon_1}, \end{aligned} \tag{2}$$

in which B stands for the magnitude of the magnetic field, θ denotes the angle between the field vector and the *c*–axis of the superconductor. The others correspond to the fit parameters, and a nonlinear fit based on the Levenberg–Marquardt algorithm was implemented for the experimental data measured for the SCS-4050-AP tape (SP-26) [23]. Table 2 lists the fit parameters in detail. In addition, we ignore the shielding effect in the LTS coil windings and specify their electric resistivities as a constant value of material copper at liquid helium temperature, i.e., $2\times10^{-11}\ \Omega\,\mathrm{m}$. Moreover, a very large resistivity of $1\ \Omega\,\mathrm{m}$ is set for the air region.

Due to the high ratio of the width to thickness of the mesh element (typically 40-80), simulating the electromagnetic behaviors in a stack of REBCO tapes or a stack of pancake coils with modeling the actual thickness of the superconducting layer is rather time-consuming [18, 24-26]. An effective and simple way is to artificially expand the thickness of superconducting layer to the overall thickness of one turn of the co-wound tape. Consequently, the radial gaps between adjacent superconducting

Table 2. Fit parameters in equation (2).

Parameter	Value
k_0	8870
k_1	18500
α_0	1.30
α_1	0.809
β_0	13.8
β_1	13.8
φ_1	-0.180° *
c_1	2.15
ε_1	0.6

*This nonzero value implies the maximum of $I_c(\theta)$ deviates from the *ab*-plane, but it is so small that we ignored it in the simulations for simplicity.

layers in the original geometry vanish and the expanding superconducting layers unite as a bulk, as shown in figure 2(b). Accordingly, the critical current density in equation (1) should be replaced with the engineering critical current density, i.e.,

$$J_{c,e}(B,\theta)=\frac{I_c(B,\theta)}{wD}, \tag{3}$$

where $I_c(B,\theta)$ corresponds to equation (2), and w, D denote the width and thickness of the co-wound tape, respectively. Furthermore, several adjacent turns in a pancake with a large number of turns can be combined into one 'engineering turn' attributed to their similar current density distributions (see figure 2(c)). If we assume that the sheet current density is uniform over the radial thickness of the pancake bulk, the thickness of the engineering turn even can be adjusted more flexibly and is no longer restricted to the integral multiples of the thickness of co-wound tape. Finally, a current constraint with integral form is applied on each engineering turn as the boundary condition of the solving system:

$$\int_{\Omega_k} J_{\varphi}(t)d\Omega_k = D_k I(t)/D, \tag{4}$$

where Ω_k denotes the cross-section domain of the kth engineering turn, D_k the thickness of the engineering turn and $I(t)$ the time-dependent applied current in one original turn. Similar integral current constraints are applied on the LTS coil windings as well.

Each of the bulk-like pancakes in the model is meshed to 50 engineering turns and the first-order edge element [27] with rectangular shape is adopted for discretization. The general form PDE module of the commercial finite element software Comsol Multiphysics [28] is used to solve the electromagnetic field distributions in the system.

2.2. Mechanical models

Two two-dimensional axisymmetric mechanical models for the REBCO high field coil will be modeled and compared in this paper. The one is the bulk model which treats a pancake as a continuum bulk. A similar idea was widely used for the stress analysis in the plane stress state, namely, treating the pancake as a continuum disk without height along the axial direction [10-16]. Because our REBCO high field coils were wound in the dry-wound approach [21], the adjacent turns in a pancake may separate from each other during deformation. Therefore, a new discrete contact model which considers the behaviors of contact and separation between adjacent turns is proposed as well in order to obtain more reasonable results.

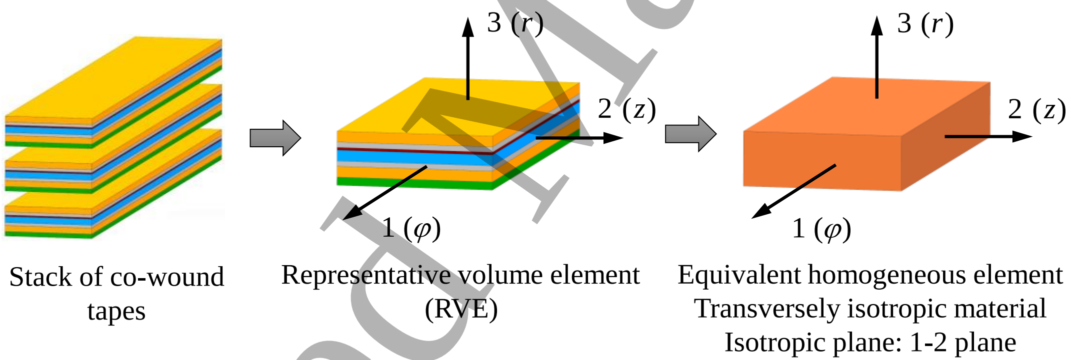

Figure 3. Equivalent homogeneous concept for the REBCO conductor/SS co-wound tape in a pancake.

2.2.1. Bulk model

The REBCO conductor/SS co-wound tape in the pancake has a laminated architecture and thereby can approximate to an equivalent homogeneous material with transverse isotropy, for which the 1-2 plane is the isotropic plane, as shown in figure 3. This transversely isotropic homogeneous material follows a material constitutive relation in the form of

$$\begin{bmatrix} \varepsilon_1 \\ \varepsilon_2 \\ \varepsilon_3 \\ \gamma_{23} \\ \gamma_{31} \\ \gamma_{12} \end{bmatrix} = \begin{bmatrix} S_{11} & S_{12} & S_{13} & 0 & 0 & 0 \\ S_{12} & S_{11} & S_{13} & 0 & 0 & 0 \\ S_{13} & S_{13} & S_{33} & 0 & 0 & 0 \\ 0 & 0 & 0 & S_{44} & 0 & 0 \\ 0 & 0 & 0 & 0 & S_{44} & 0 \\ 0 & 0 & 0 & 0 & 0 & 2(S_{11}-S_{12}) \end{bmatrix} \begin{bmatrix} \sigma_1 \\ \sigma_2 \\ \sigma_3 \\ \tau_{23} \\ \tau_{31} \\ \tau_{12} \end{bmatrix}, \tag{5}$$

where the column vectors on the left and right sides of equation (5) stand for the strain and stress components, respectively. The subscripts $(1,2,3)$ correspond to (φ, z, r) in the cylindrical coordinate system, respectively. The 6×6 square matrix in equation (5) is the elastic compliance matrix, which has the symmetrical property and only five independent components exist. Those nonzero compliance coefficients can be expressed by a series of equivalent elastic constants of the transversely isotropic homogeneous material as

$$S_{11} = \frac{1}{\bar{E}_1}, \; S_{12} = -\frac{\bar{\nu}_{21}}{\bar{E}_1}, \; S_{13} = -\frac{\bar{\nu}_{31}}{\bar{E}_3}, \; S_{33} = \frac{1}{\bar{E}_3}, \; S_{44} = \frac{1}{\bar{G}_{23}}. \tag{6}$$

The equivalent Young's modulus components $\bar{E}_1$ and $\bar{E}_3$, equivalent Poisson's ratio components $\bar{\nu}_{21}$ and $\bar{\nu}_{31}$, and equivalent shear modulus component $\bar{G}_{23}$ depend on the elastic constants and thickness proportions of the component materials in the laminated composite co-wound tape. The formulated relations are presented in equation (7) and the derivations in detail are given in the Appendix.

$$\begin{aligned} &\bar{E}_1 = \sum_m c_m E_m, \quad \frac{1}{\bar{E}_3} = \sum_m \frac{c_m}{E_m}, \quad \bar{\nu}_{21} = \frac{\sum_m c_m \nu_m E_m}{\sum_m c_m E_m}, \\ &\bar{\nu}_{31} = \frac{\bar{E}_3}{\bar{E}_1} \sum_m c_m \nu_m, \quad \frac{1}{\bar{G}_{23}} = \sum_m \frac{c_m}{G_m}, \end{aligned} \tag{7}$$

in which c_m represents the thickness proportion for the *m*th component, and E_m, ν_m, G_m are the Young's modulus, Poisson's ratio, and shear modulus for the *m*th component, respectively. Table 3 summarizes the material components in the co-wound tape and the corresponding elastic constants at the liquid helium temperature. Note that equations (5)-(7) present a completed elastic constitutive relation for the transversely isotropic homogeneous material in three-dimensional spatial stress/strain state, which can be used straightforward for three-dimensional stress/strain analysis or be regressed to lower-dimensional situations. In addition, the nonlinear elastoplastic property is not considered in this paper.

Table 3. Material components and elastic constants in co-wound tape at $4.2\ \mathrm{K}$.

Component	Thickness (μm) [a]	E_m (GPa)	ν_m	G_m (GPa)
Copper	100	40 [b]	0.3	15
Hastelloy C-276	50	210 [29]	0.3	81
REBCO	1	180 [30, 31]	0.3	69
Ag+Buffer	4	90 [32]	0.3	35
Insulated SS tape	32	156 [c]	0.3	60

[a] Ideal specifications of the component thicknesses are used in our model. The variations of thicknesses over the total length of the tapes in a pancake and the assembling clearances between turns are ignored. Therefore, the outer radius of the pancake in our model is 65.6 mm instead of 70 mm as presented in table 1.
[b] Adjusted based on the secant modulus of the reference stress-strain curve for the 32-T REBCO conductor at a strain of 0.4% [22].
[c] The insulated SS tape consists of a bare SS tape with a thickness of $25\ \mu\mathrm{m}$ and a coated sol-gel insulated layer with a thickness of $3.5\ \mu\mathrm{m}$ on the both sides. The tensile stiffness of the latter is neglected and the Young's modulus is scaled by a factor of $25/32$ from the original $200\ \mathrm{GPa}$ [32] for stainless steel.

We need to point out that the Young's modulus of copper stabilizer given in table 3 is much lower than its realistic value (85 GPa at 77 K [33]). This treatment originates from the nonlinear mechanical property of the laminated composite REBCO conductor. Uniaxial tension tests [22, 33] showed that the REBCO coated conductor with a 100 μm-thickness copper stabilizer had a nonlinear stress-strain relation even at early deformation stage, the slope decreasing with increasing strain. This is attributed to the fact that the yielding of the copper stabilizer starts at a much lower stress level compared with that of the Hastelloy substrate [33]. In this paper, a linear constitutive model is used, neglecting the nonlinear behavior. Employing the realistic Young's modulus for copper stabilizer will result in significant underestimations on the hoop strain at high hoop stress levels. Therefore, we adjust the Young's modulus of copper so that the conductor can deform along a secant path of 0.4% strain based on the reference stress-strain curve of the 32-T REBCO conductor, as shown in figure 4.

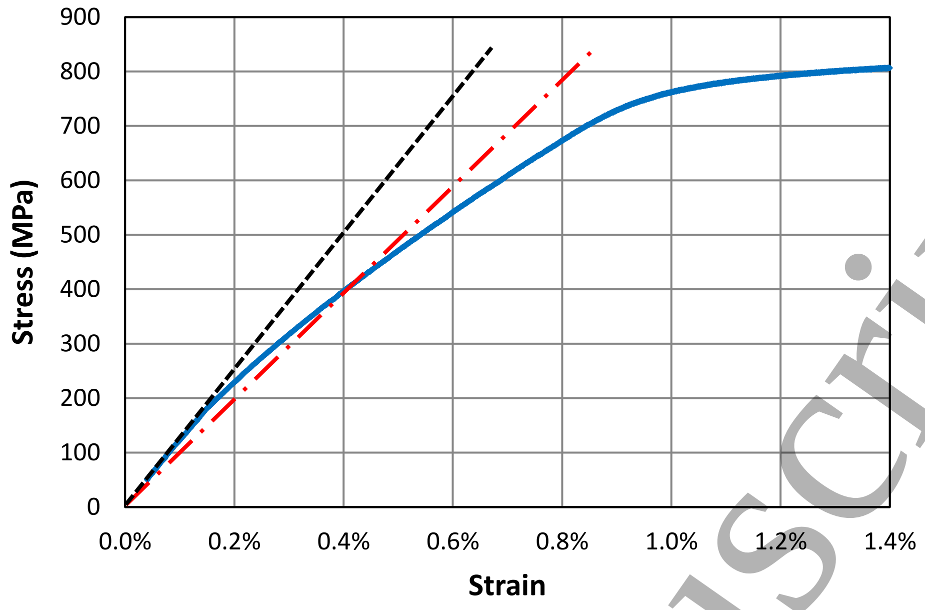

Figure 4. (Solid line) the reference stress-strain curve for the 32-T REBCO conductor at 4.2 K [22]. The dash line illustrates the initial slope of the curve and the dash dot line illustrates the secant stress-strain relation used in the simulations.

Besides the constitutive relation (5), the stress equilibrium equation (8) and kinematic equation (9) are indispensable for constituting the governing equations of the problem of elastic mechanics:

$$\left.\begin{aligned}&\frac{\partial\sigma_r}{\partial r}+\frac{\partial\tau_{zr}}{\partial z}+\frac{\sigma_r-\sigma_\varphi}{r}+f_r=0,\\&\frac{\partial\sigma_z}{\partial z}+\frac{\partial\tau_{zr}}{\partial r}+\frac{\tau_{zr}}{r}+f_z=0,\end{aligned}\right\} \tag{8}$$

$$\varepsilon_r=\frac{\partial u}{\partial r},\ \ \varepsilon_\varphi=\frac{u}{r},\ \ \varepsilon_z=\frac{\partial w}{\partial z},\ \ \gamma_{zr}=\frac{\partial u}{\partial z}+\frac{\partial w}{\partial r}. \tag{9}$$

Here the two-dimensional axisymmetric formulation are presented directly and u, w denote the displacements of radial and axial directions, respectively.

Once the distributions of the magnetic field and current density are worked out from the electromagnetic model, the Lorentz force $\mathbf{f}_\mathrm{L}$ in the form of equation (10) will be applied on the engineering turns in the pancakes.

$$\mathbf{f}_\mathrm{L}=\mathbf{J}\times\mathbf{B}=f_r\mathbf{i}_r+f_z\mathbf{k}=J_\varphi B_z\mathbf{i}_r-J_\varphi B_r\mathbf{k}, \tag{10}$$

in which f_r and f_z represent the radial and axial components of the Lorentz force (corresponding to the same notations in equation (8) as well), $\mathbf{i}_r$ and $\mathbf{k}$ represent the unit vectors of radial and axial directions, respectively.

A simple boundary condition is taken into account here, i.e., we constrain the axial displacement for the bottom boundary of the bulk-like pancake, and the other boundaries are able to move freely. The winding tension, the overband around the outer radius of the pancake, and the residual stress resulting from the thermal contraction during cool down are not considered currently.

Equations (5)-(10) in association with the aforementioned boundary condition will be solved numerically by the structural mechanics module embedded in the same simulation platform, i.e., Comsol Multiphysics. The second-order Lagrange element with rectangular shape is employed for discretization (which is also employed in the following discrete contact model).

2.2.2. Discrete contact model

The basic governing equations and boundary conditions still work on the discrete contact model. Here the 50 engineering turns in a pancake, as depicted in the electromagnetic model, are refined into 200 turns after the calculation of electromagnetic fields is completed. Contact pairs are defined between adjacent turns in a pancake. Moreover, the friction force between adjacent turns is ignored due to three reasons: (1) The influence of friction on determining the hoop stress can be ignored; (2) The values of the friction coefficients are unknown yet currently; (3) Adding friction to the contact problem will increase the computation time significantly, and even cause convergence problems [34]. The simulation of the behaviors of deformation, contact and separation for the bundle of discrete turns in a pancake is implemented by the structural mechanics module of Comsol Multiphysics with the 'contact' sub-module being employed. The built-in penalty method is chosen as the contact algorithm. That method is rather simple and robust, which, roughly speaking, is on a basis of adding a stiff spring between contacting boundaries, active only in compression [34]. Furthermore, the Lorentz force is gradually increased to the final value by several load steps in order to avoid non-convergence.

3. Model study

In this section, we will discuss the influences of shielding current on the mechanical responses in the HTS coil, as well as study the differences of the simulation results from the aforementioned two mechanical models.

The inner HTS coil and the outer LTS coils are charged independently [21, 22]. In this paper, the latter is charged first to generate a 15 T background field in its bore during the electromagnetic simulation. After the background field becomes steady, the former is ramped up to a goal operating current of 180 A with a ramp rate of 1 A/s unless otherwise stated and the central field rises to 25.6 T at that turning-point moment. Afterwards, the mechanical responses of the HTS coil at that moment are analyzed by means of the two mechanical models in the high field condition.

3.1. Distributions of electromagnetic field and Lorentz force

Figure 5 gives the distributions of magnetic field components and current density in the 20/70 REBCO coil as the coil system is right fully charged, in which the symbols '#1', '#10' and '#20' on the left of the coil indicate the numbering sequence for the pancakes from the midplane to the end of the coil winding in the half-built model. One can see the axial field distribution has a straightforward characteristic of descending with increasing radius. Moreover, the radial field ascends as the spatial position moves away from the midplane and the end pancake suffers the highest radial field among the pancake stack. One can also see that the radial field cannot thoroughly penetrate the pancakes and the magnitude of radial field decays towards the interiors of the pancakes. The physical reason is attributed to the shielding currents induced in the superconducting tapes, as shown in figure 5(c). It can be seen that a pair of azimuthal currents flowing along opposite directions appears in the turns, which generates an opposite magnetic field to resist the radial field from penetrating into the pancakes. Due to the increasing of the radial field along the direction from pancakes #1 to #20, the shielding current behaves more conspicuously in the pancake with a larger pancake sequence number. Note that figure 5(c) presents the superposition consequence of the shielding current and the applied current, rather than the former individually. Similar current density distributions have been found by using other simulation methods, such as the minimum magnetic energy variation method [19] and iterative multi-scale method [20]. We can also see the current density profiles along the axial direction in figure 17, which will be presented in the next section.

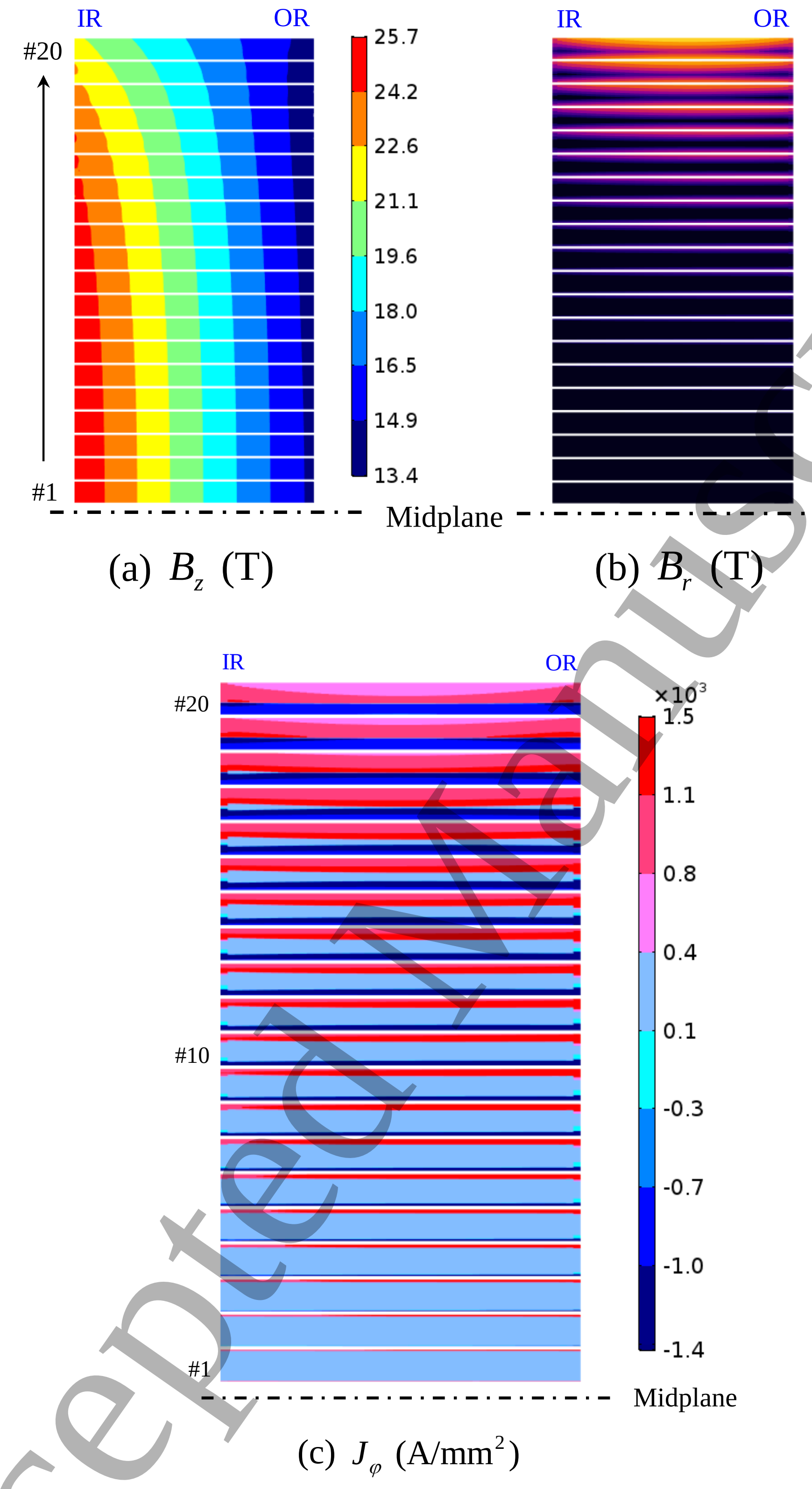

Figure 5. Distributions of (a) axial field, (b) radial field and (c) current density in the 20/70 REBCO coil as the coil system is fully ramped up. 'IR' and 'OR' indicate the positions of inner radius and outer radius of the coil, respectively.

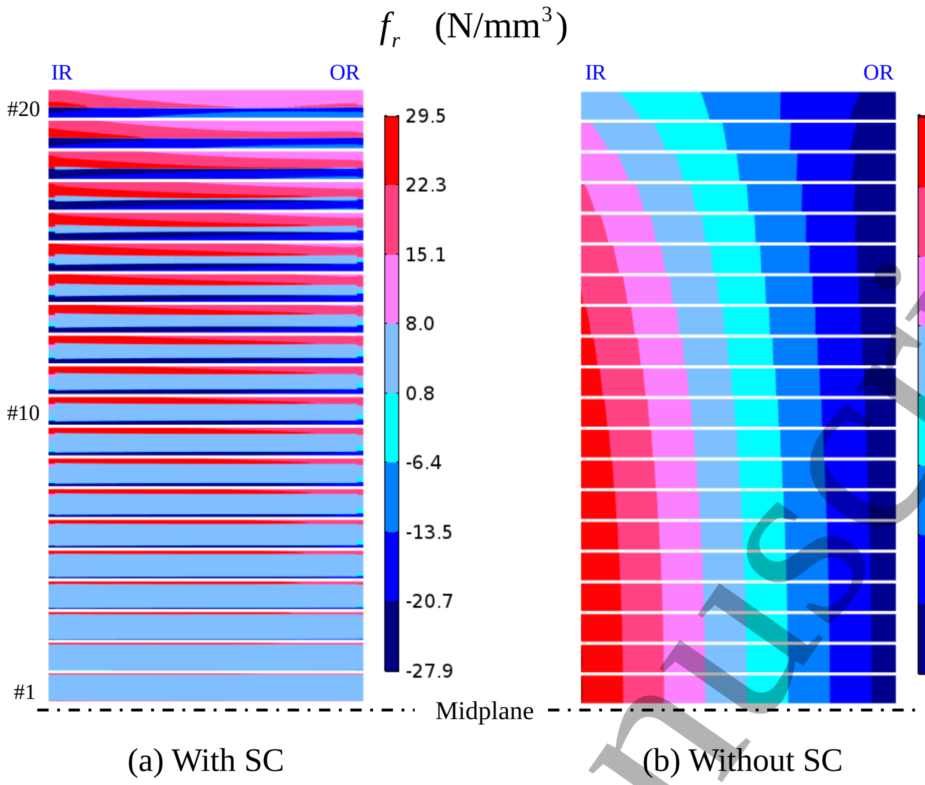

Figure 6. Distributions of radial Lorentz force for (a) 'With SC', i.e., the case with shielding current and (b) 'Without SC', i.e., the case without shielding current.

The corresponding Lorentz force distribution in the coil is shown in figure 6(a). Moreover, figure 6(b) gives the corresponding result for the case of neglecting the shielding current behavior for comparison, which is implemented by treating the HTS coil as a copper coil, namely, employing the resistivity of copper instead of the superconducting one. One can find that the distributions for the two cases are totally different. For the case with shielding current, it is apparent that the distribution characteristics of the shielding current play the dominant role on determining the distribution pattern of the Lorentz force. A pair of radial Lorentz forces with opposite directions act on the turns. The radial shear will make the turns experience a significantly nonuniform radial deformation in the tape width direction. Larger local hoop stresses will be generated at the top edges of the turns and smaller local hoop stresses will be generated at the bottom edges of the turns. For the case without shielding current, the distribution pattern of the Lorentz force is exclusively determined by the magnetic field distribution since the current density distribution is uniform in that case. The Lorentz force exclusively points towards the direction of radial expanding and it declines with increasing radius. The deformation of radial shear here can be neglected compared to that for the case with shielding current. In addition, one can also find that the case with shielding current has larger magnitudes of the Lorentz force than the case without shielding current, which originates from the higher current densities in the former. This feature implies that higher local hoop stresses could be generated in the turns due to the shielding current effect.

Furthermore, figure 7 gives the profiles of the radial Lorentz force along the radial direction in three typical pancakes, in which three key local positions in the turn (i.e., the top, the middle and the bottom as illustrated in the legend) are picked for the data output. One sees that the Lorentz force decreases with increasing radius for both cases with and without shielding current, which is the consequence of the decline of the axial magnetic field along the same direction. The force magnitudes in the case without shielding current are obviously smaller than those in the case with shielding current, and the curves for different latitudes in each pancake are almost overlapping. For the case with shielding current, the distribution characteristics are complicated. In pancake #20, the Lorentz forces on the middle latitude are higher than those on the top latitude. However, the feature is opposite in pancake #10. Besides, no negative Lorentz forces exist in pancake #1. Those characteristics can be understood by means of the corresponding current density distributions, which are shown in figure 8.

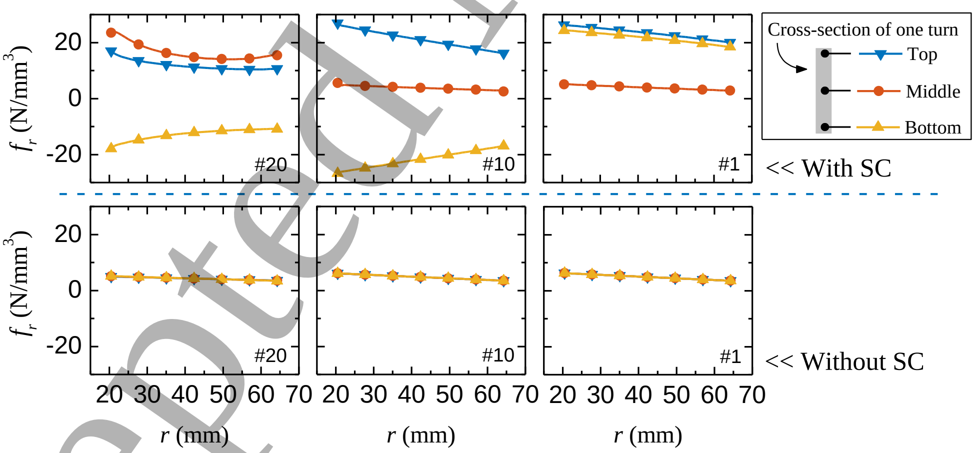

Figure 7. Profiles of the radial Lorentz force along the radial direction in pancakes #1, #10 and #20. The upper three plots correspond to the case with shielding current and the lower three plots correspond to the case without shielding current. The legend illustrates the corresponding latitude locations of the profile curves in every pancake.

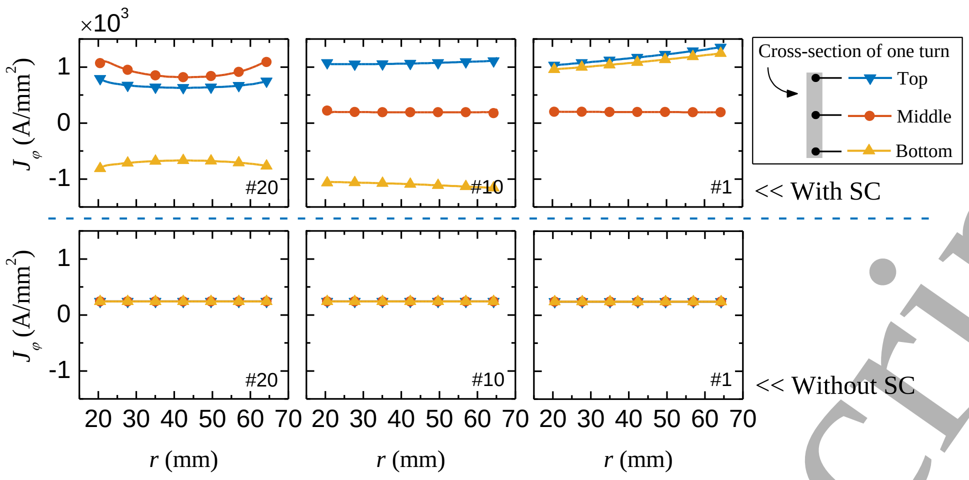

Figure 8. Profiles of the current density along the radial direction in pancakes #1, #10 and #20.

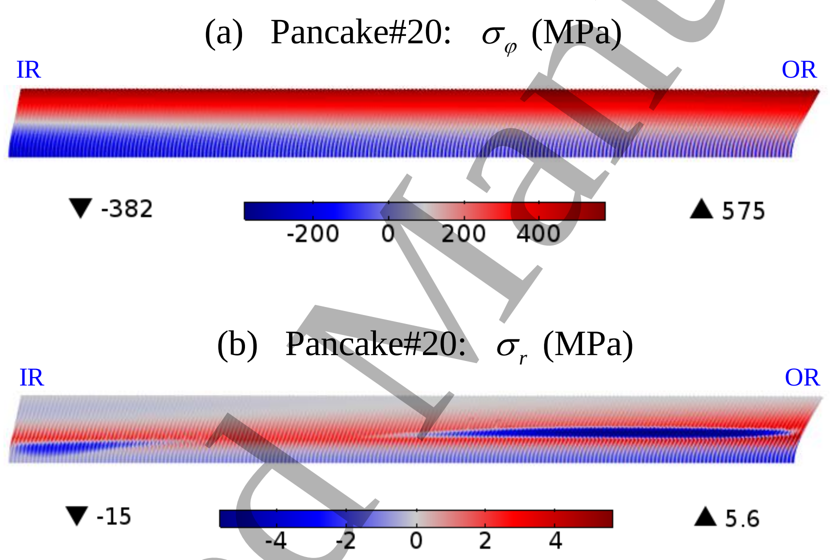

Figure 9. Distributions of (a) hoop stress and (b) radial stress in pancake #20 based on the discrete contact model, where the shielding current behavior is taken into account. The deformation scale factor is 5 in both plots.

3.2. Mechanical responses in discrete contact model

Now we take pancake #20 as an example to detail the characteristics of mechanical responses in a pancake. Figure 9 demonstrates the contour plots of the hoop and radial stresses for this pancake based on the discrete contact model while taking into account the shielding current behavior. Different from the case neglecting the shielding current behavior, it can be seen that the pancake here experiences a nonuniform radial deformation along the axial direction. Figure 9(a) shows that the top edges of the turns in the pancake are subjected to high tensile hoop stresses and the bottom edges of the turns are subjected to compressive hoop stresses. Moreover, figure 9(b) shows the radial stress distribution has complicated features. First, compressive radial stresses appear at the bottom zone of the pancake, which is the consequence of the bottom edges of the turns moving towards the central axis due to the radial shear. However, the compression behavior is not obvious at the top zone of the pancake. Second, tensile radial stresses appear at the middle zone of the pancake. This is because the upper and lower parts of the turns move towards the opposite directions and thereby tensile stresses are generated in the middle parts of the interiors of the turns. Third, one can see an obvious compressive stress zone which is near the middle latitude of the pancake and also close to the outer radius. That implies the complexity of mechanical response of the multibody system and we think the compressive stress zone is attributed to the adjacent turns being compressed by each other as the upper parts of the turns move outwards. Figure 10 gives a series of more detailed results to help us understand the deformation response. From figure 10(a), one sees that for the case with shielding current, the local hoop stress at the top edge of the turn basically keeps a constant along the radial direction and increases a little in the vicinity of the outer radius; the value of local hoop stress on the middle and bottom latitudes monotonously increases with increasing radius. Therefore, the highest tensile and compressive hoop stresses are located at the top edge of the outermost turn and the bottom edge of the innermost turn, respectively. Moreover, a hoop stress profile in the case without shielding current is also drawn in figure 10(a). Note that since the curves corresponding to different latitudes are almost overlapping in this case, only the curve for the middle latitude is presented. In addition, the hoop stress estimation based on the classic formula $\sigma_\varphi(r) = r \cdot J_\varphi(r) \cdot B_z(r)$ is presented as well for comparison, in which J_φ and B_z take the results without considering the shielding current behavior. It is found that the aforementioned two curves agree well with each other and they are slightly higher than the curve corresponding to the middle latitude of the pancake in the case with shielding current; however, their results are significantly lower than the local stresses at the top edge of the pancake in the case with shielding current. Furthermore, we found the analytical formula of $rJ_\varphi B_z$ cannot give an adequate estimation for the local hoop stress even though the electromagnetic field results of considering the shielding current behavior are used.

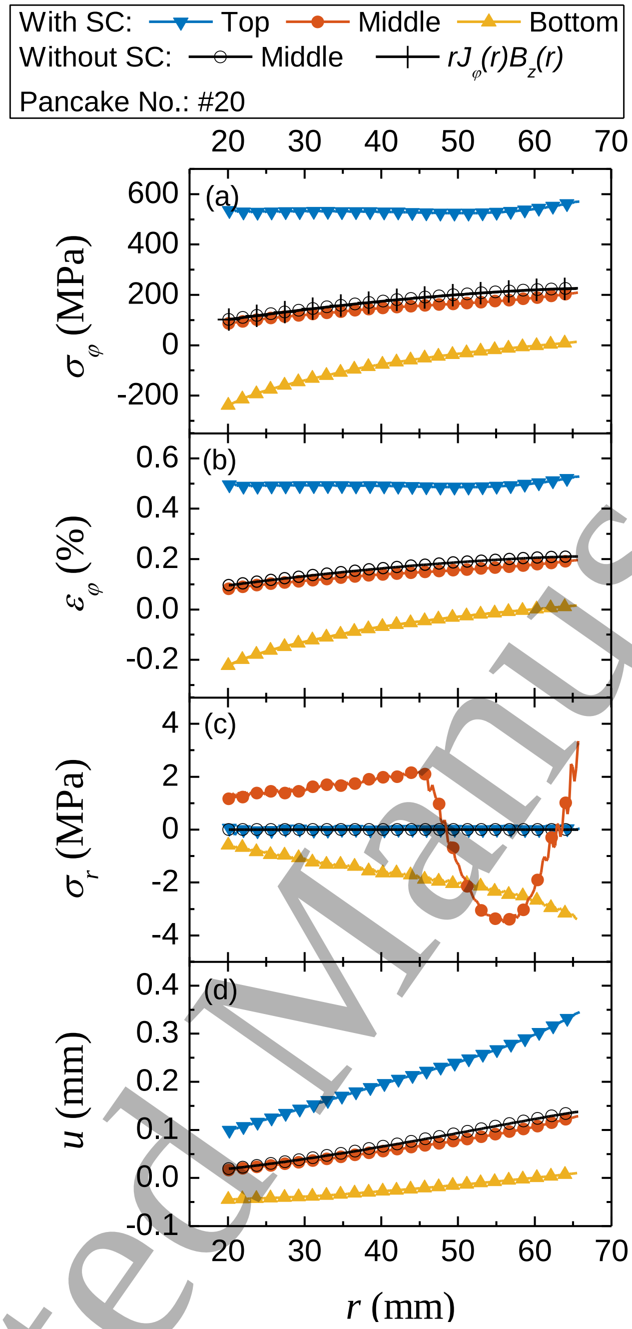

Figure 10. Profiles of (a) hoop stress, (b) hoop strain, (c) radial stress, and (d) radial displacement on different latitudes in pancake #20 based on the discrete contact model.

From figure 10(b), it can be seen that the hoop strain profiles have consistent features with the stress ones. Figure 10(c) gives radial stress profiles on different latitudes of the pancake. For the case with shielding current, one can see the radial stresses at the top edge of the pancake are negligible under that vertical coordinate scale; a complicated non-monotonous distribution exists on the middle latitude of the pancake, which can be understood by recalling figure 9(b); the radial stresses at the bottom edge of the pancake are compressive and the compressive stress ascends towards the outer radius direction. For the case without shielding current, the radial stresses are negligible compared to the results with shielding current. Figure 10(d) gives the radial displacement profiles on different latitudes of the pancake. For the case with shielding current, the value of radial displacement increases with increasing radius and increasing latitude location; for the case without shielding current, the curve is slightly higher than the middle one in the case with shielding current. Furthermore, we give the hoop strain distributions in the direction of tape width at different radial positions in pancake #20, as shown in figure 11. It is clear that the value of hoop strain increases from the bottom edge to the top edge in the case with shielding current; however, the hoop strains in the case without shielding current are almost the same in each turn. One can see the hoop strains at the middle of tape width are close to each other for the two cases. Roughly speaking, the nonuniform strain distribution in the case with shielding current can be deemed to be a consequence of the combination of a pure stretching along the length direction and a pure bending in the tape plane.

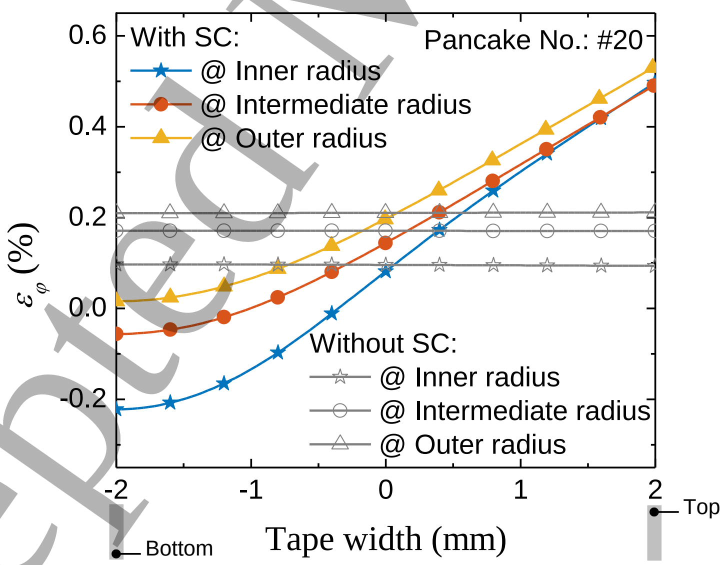

Figure 11. Hoop strain distributions in the direction of tape width at different radial positions in pancake #20 based on the discrete contact model.

Figure 12 summarizes the maximum local hoop stresses in every pancake, where only the data with even pancake sequence numbers are presented for brevity. It indicates that neglecting the shielding current behavior results in a significant underestimation on the local hoop stress. The percentages on the top of the columns denote the relative deviations between the data of the two cases, which are calculated by $\left(\sigma_{\varphi,\max}^{\text{with SC}} - \sigma_{\varphi,\max}^{\text{without SC}}\right) / \sigma_{\varphi,\max}^{\text{without SC}}$, where $\sigma_{\varphi,\max}^{\text{with SC}}$ and $\sigma_{\varphi,\max}^{\text{without SC}}$ represent the maximum local hoop stresses with and without shielding current in every pancake, respectively. For the case without shielding current, the maximum local hoop stresses nearly keep a constant of $225\,\text{MPa}$ in every pancake. This point can be easy to understand by means of the analytical formula of $\sigma_\varphi = rJ_\varphi B_z$: the maximum local hoop stresses are located in the outermost turn for every pancake and the B_z there changes a little along the axial direction; therefore, the stresses in every pancake are close to each other. For the case with shielding current, the maximum local hoop stress in pancake #14 is up to $766\,\text{MPa}$. The nonuniform distribution of the maximum local hoop stresses originates from the difference of the torques acting on the turns of the pancakes. And the latter is dominated by the difference of the current density distributions in every pancake, as shown in figure 17. The maximum local hoop stress does not monotonously increase with increasing pancake sequence number and the highest local hoop stress is located in a certain pancake near the end of the coil winding. The reason is that although pancake #20 suffers a higher radial magnetic field and thereby the shielding current behavior is more conspicuous, the higher radial magnetic field leads to a severer degeneration on the critical current density, which gives rise to lower current densities at the top and bottom edges of the pancake. Consequently, the torques acting on the turns of the pancake are not the strongest and thus the highest local hoop stress does not appear in it.

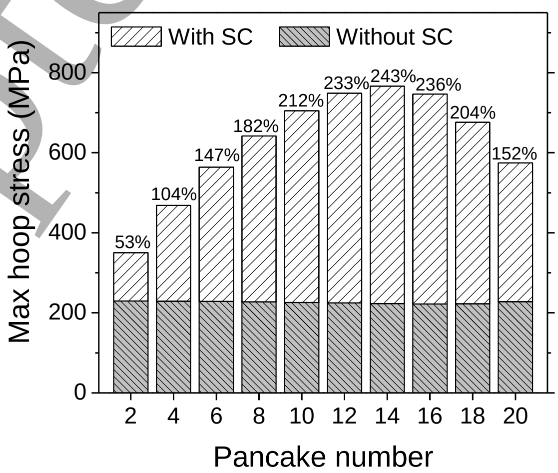

Figure 12. Maximum local hoop stresses in pancakes based on the discrete contact

model.

3.3. Mechanical responses in bulk model

This subsection will present the mechanical response results simulated by the bulk model and these results will be compared with those simulated by the discrete contact model. Only the case with shielding current is discussed in this subsection.

Figure 13 shows the contour plots of the hoop and radial stresses for pancake #20 based on the bulk model. It can be seen that the radial shearing deformation resulting from the pair of opposite Lorentz forces is negligible and no compressive hoop stress is found in the pancake. The tensile hoop stress descends monotonously towards the outer radius. Moreover, large tensile radial stress appears in the pancake, which implies the bulk model forcibly prevents the turns from separating from each other.

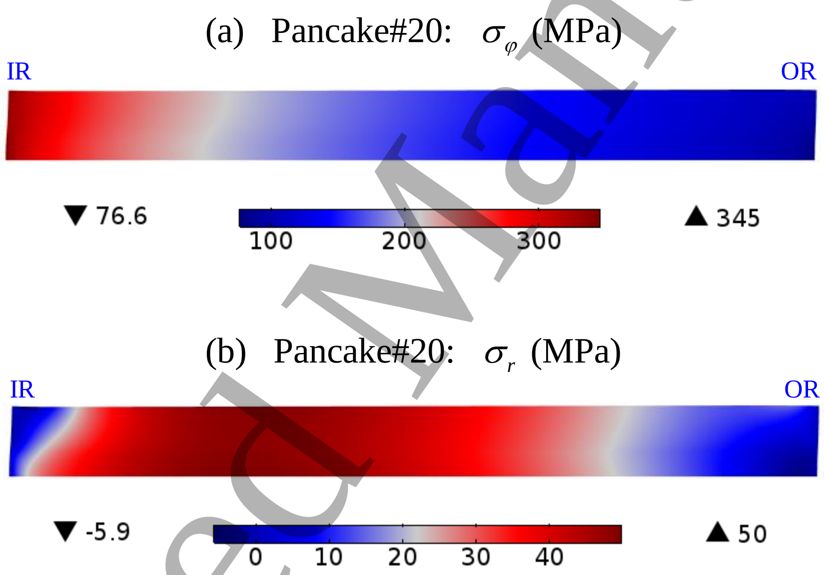

Figure 13. Distributions of (a) hoop stress and (b) radial stress in pancake #20 based on the bulk model, where the shielding current behavior is taken into account. A deformation scale factor of 40 is used here.

Similar to figure 10, figure 14 gives the profiles of hoop stress, hoop strain, radial stress and radial displacement in pancake #20 based on the bulk model, in which the corresponding curves calculated from the discrete contact model are redrawn for comparison. It is clear that the two models give very different results. In the bulk model, the stresses and displacement are almost uniform in the direction of tape width. Namely, the nonuniform responses cannot be embodied. From figure

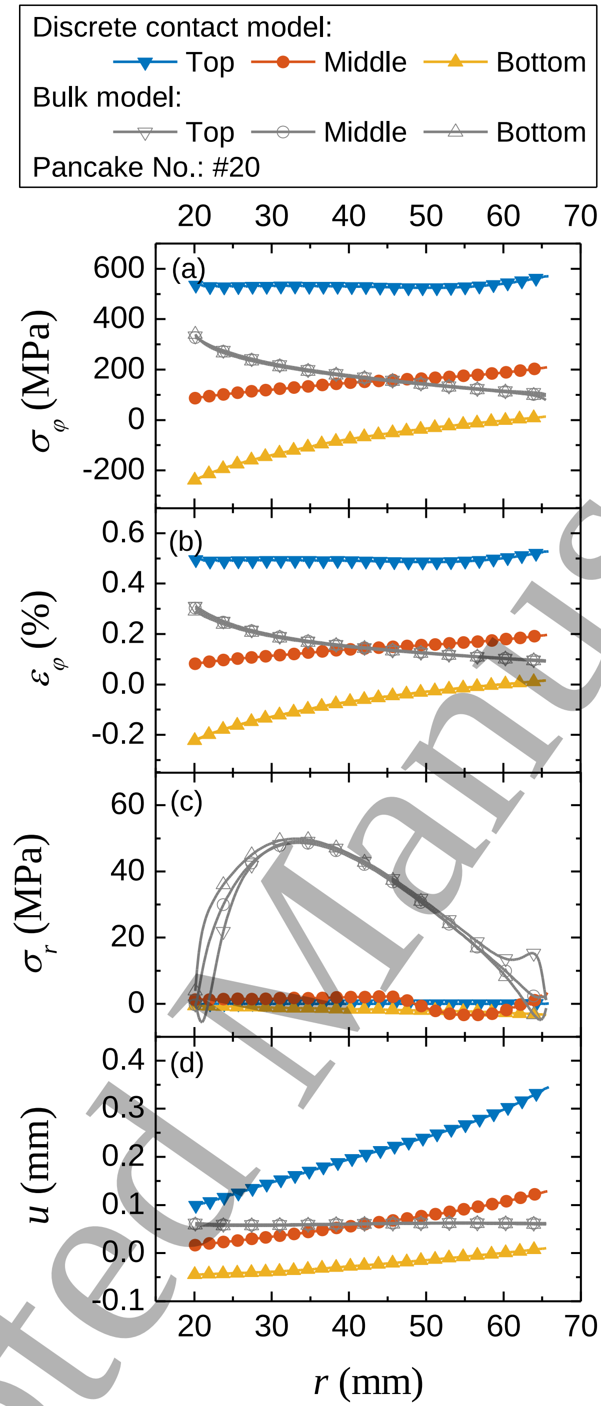

Figure 14. Profiles of (a) hoop stress, (b) hoop strain, (c) radial stress, and (d) radial displacement on different latitudes in pancake #20 based on the bulk model. The corresponding profiles based on the discrete contact model are redrawn here for comparison.

14(a), one sees that the hoop stress declines with increasing radius in the bulk model (noting that the shielding current behavior is taken into account in our bulk model), which is qualitatively consistent with the feature reported by the works [10, 11] which did not consider the shielding current behavior. However, the results of the discrete contact model indicate that the local hoop stress has a rising tendency towards the outer radius. The corresponding hoop strain values can be seen in figure 14(b). From figure 14(c), one sees that the radial stresses are almost all at the tensile state in the bulk model, mostly larger than $10\ \mathrm{MPa}$. However, the transverse delamination tests of YBCO coated conductors showed that the critical transverse tensile stress was about $10\ \mathrm{MPa}$ [35]. It indicates that the bulk model forcibly restricts the separation of adjacent turns and the simulation deviates from the reality for dry-wound pancakes. From figure 14(d), it is found that the radial displacements approximate to a constant in the bulk model. However, the value of radial displacement increases with increasing radius in the discrete contact model. In summary, the bulk model deviates from the fact that adjacent turns in dry-wound pancakes could separate from each other during the deformation and movement. It considerably suppresses the radial shearing deformation of the pancake and the maximum local hoop stress is underestimated.

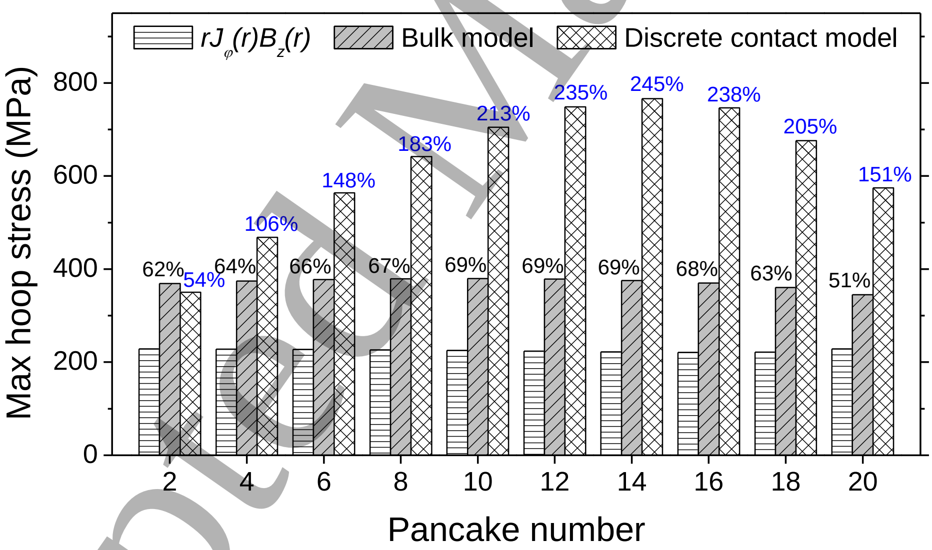

Figure 15. Maximum local hoop stresses in pancakes based on the classic formula (without SC), bulk model (with SC) and discrete contact model (with SC), respectively.

Furthermore, figure 15 compares the maximum local hoop stresses in pancakes among the classic formula $\sigma_{\varphi}(r) = r \cdot J_{\varphi}(r) \cdot B_z(r)$, bulk model and discrete contact model. The shielding current behavior is taken into account for the two models, while the traditional formula estimation does not consider it. The percentages on the top of the columns denote the relative deviations referring to the results of the classic formula. Two findings can be concluded. First, the maximum local hoop stresses for the bulk model basically lie on a same level and so do those for the classic formula. The formers are significantly higher than the latters because of the contribution of shielding current to the Lorentz force. Second, the results of the bulk model are lower than those of the discrete contact model (expect for pancake #2), and the deviations are still significant.

3.4. Discussions

The degradation of critical current can occur at a tensile stress/strain of $\geq 575\,\mathrm{MPa}$ / $\geq 0.65\%$ for the REBCO tape used in the NHMFL 32 T all-superconducting magnet [22]. Our simulation results of the discrete contact model show that the high local hoop stress/strain originating from the shielding current is very likely to cause the plastic deformation in the REBCO tape and the superconducting layer in the tape may be damaged in part. The overband around the outer radius of the pancake and the winding tension, which are adopted in reality, seem effective to suppress the hoop stress currently. But the high local hoop stress caused by the shielding current is still a very noticeable issue as the service time of the magnet accumulates and also in the next exploration activities of developing a stronger superconducting magnet. In addition, note that our calculations are based on the assumption of linear deformation. The simulation of nonlinear plastic deformation remains to be implemented in the future.

The nonuniform hoop strain in the direction of tape width is a new noticed problem in the application of REBCO tapes. Although the hoop strain at the middle of a turn is much lower than the permissible limit, the high local hoop strain at the top edge of a turn could initiate the microcracks nearby and even facilitate the expanding of the microcracks, which will lead to the degeneration problem of the critical current. A recent tensile test which brought about a combined strain mode of uniaxial stretching and in-plane bending in REBCO tapes showed an earlier degeneration than the pure stretching [36]. More experiments with elaborate designs and relevant theories are expected in order to understand the correlation between the high local hoop strain and current transport property, or namely, what the limit for the tape to tolerate the nonuniform deformation is.

4. Factor study

In this section, we will study the influences of a couple of practical factors on the shielding current and hoop stress based on the discrete contact model. The factors include the n-value, ramp rate, and operating mode of the REBCO coil winding.

4.1. n-value and ramp rate

During the activities of developing the HTS insert for the 32 T magnet, we noticed that the n-value of the REBCO conductor could vary noticeably over the total conductor length employed in the coil windings. This inspired us to see if we could reduce the hoop stress by means of controlling the n-value. Figure 16 shows the current density profiles along the axial direction at the intermediate radius of the REBCO coil winding, calculated from different n-values. The profiles correspond to the turning-point moment when the REBCO coil is ramped up to the goal operating current, 180 A. It is found that a lower n-value results in lower current density peaks in the pancakes. As a consequence, the hoop stress should decrease. Table 4 gives the variation of the maximum local hoop stress of the coil winding and it shows that the stress decreases by 6.5% from $n=35$ to $n=15$.

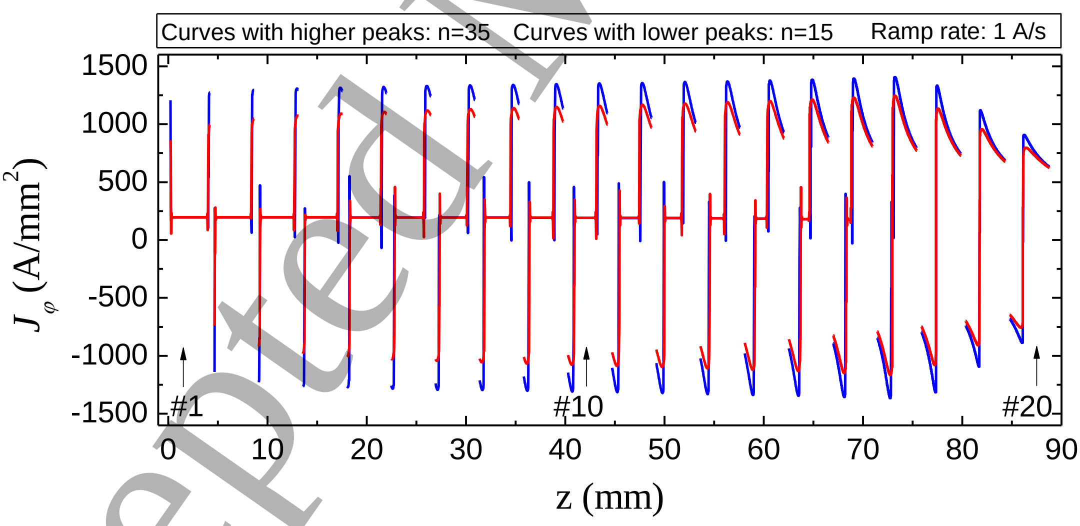

Figure 16. Current density profiles along the axial direction at the intermediate radius of the REBCO coil winding for the cases of $n=15$ and $n=35$, respectively.

Table 4. Influence of the n-value on the maximum local hoop stress of the REBCO coil winding.

n-value	Max. local hoop stress (MPa)	Located in which pancake
35	781	#14
15	730	#14
Deviation of max. local hoop stresses	↓6.5%	-

Similarly, figure 17 shows the influence of the ramp rate of the REBCO coil winding on the current density distribution at the turning-point moment. One sees that reducing the ramp rate has a slight effect on suppressing the shielding current. Furthermore, the variation of the maximum local hoop stress of the coil winding is given in table 5 as well.

It can be seen that decreasing the n-value or ramp rate can suppress the shielding current and maximum local hoop stress, but their effects are limited.

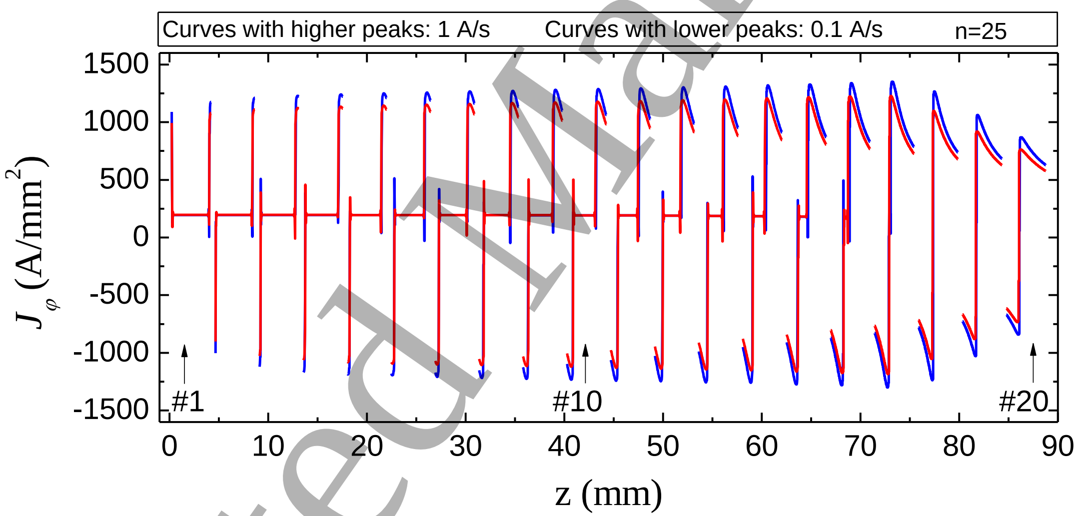

Figure 17. Current density profiles along the axial direction at the intermediate radius of the REBCO coil winding for the cases of 0.1 A/s and 1 A/s, respectively.

Table 5. Influence of the ramp rate on the maximum local hoop stress of the REBCO coil winding.

Ramp rate	Max. local hoop stress (MPa)	Located in which pancake
1 A/s	766	#14
0.1 A/s	715	#13
Deviation of max. local hoop stresses	↓6.7%	-

4.2. Operating mode of the REBCO coil winding

According to our experience, there are two ways to use the superconducting magnet in general [22]. The one is to ramp the magnet up and then hold the field for a period of time, i.e., the ramp-and-hold mode. The other is to ramp the magnet up and down nearly continuously, i.e., the ramp-up-and-down mode. Understanding the evolution behaviors of the current density and stress/strain distributions in these operating modes are very useful for the magnet design. Here we considered two cases for the simulation study.

Case I: the 15 T background field is raised up, and then a ramp-and-hold pattern is applied on the REBCO coil. Figure 18 gives the current density profiles at the intermediate radius of the REBCO coil when the REBCO coil right achieves the goal operating current of 180 A and maintains that current for one hour, respectively. It is found that the shielding current obviously decays one hour later, which indicates that the REBCO pancakes experienced the highest hoop stress level at the turning-point moment and the hoop stress gradually relaxed afterwards. The flux creep should be responsible for the degeneration phenomenon [37, 38]. Due to the creep of flux vortexes along the direction of tape width, the gradient of the magnetic field component $\partial H_r/\partial z$ reduces and hence the current density J_φ decays according to Ampere's law. Table 6 lists the maximum local hoop stresses in the REBCO coil at the corresponding moments.

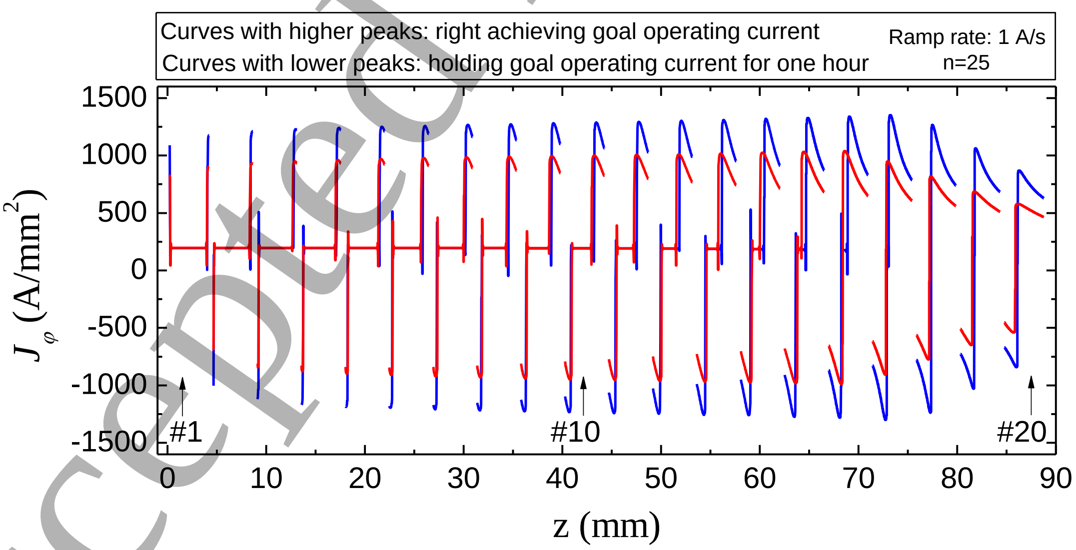

Figure 18. Current density profiles along the axial direction at the intermediate radius of the REBCO coil winding. The corresponding moments of the profiles are indicated in the legend.

Table 6. Maximum local hoop stresses in the REBCO coil winding at the specific moments.

Moment	Max. local hoop stress (MPa)	Located in which pancake
Right achieving goal operating current	766	#14
Holding goal operating current for one hour	640	#13
Deviation of max. local hoop stresses	↓16.4%	-

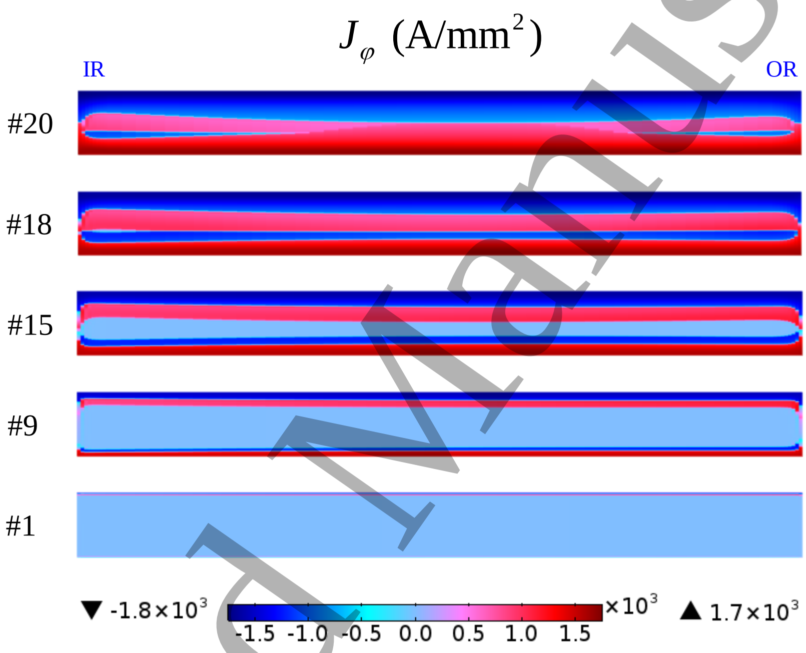

Figure 19. Current density distributions in pancakes #1, #9, #15, #18, #20 at the first fully-discharged moment for the REBCO coil.

Case II: the 15 T background field is raised up and held, and then a ramp-up-and-down pattern is applied on the REBCO coil. Figure 19 gives a set of representative contour plots of the current density in the REBCO coil at its first fully-discharged moment (noting that the background field is not discharged with the REBCO coil in this simulation). When the applied current reached the peak of 180 A and turned to ramp down, a pair of opposite shielding currents would appear at the top and bottom edges of the pancake (i.e., the blue one on the top edge and the red one on the bottom edge shown in figure 19) in order to hold back the decline of the radial field. As the applied current decreased, the fronts of this pair of shielding currents gradually penetrated towards the interior of the pancake and finally get to the pattern shown in figure 19. A current density profile along the axial direction at the intermediate radius of the REBCO coil winding for the current moment is given in figure 20.

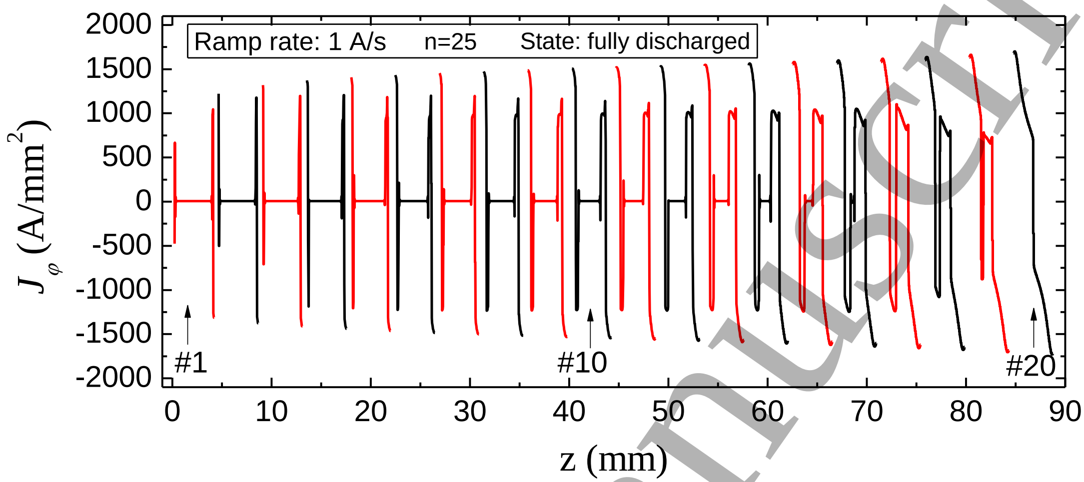

Figure 20. Current density profile along the axial direction at the intermediate radius of the REBCO coil winding at the fully-discharged moment.

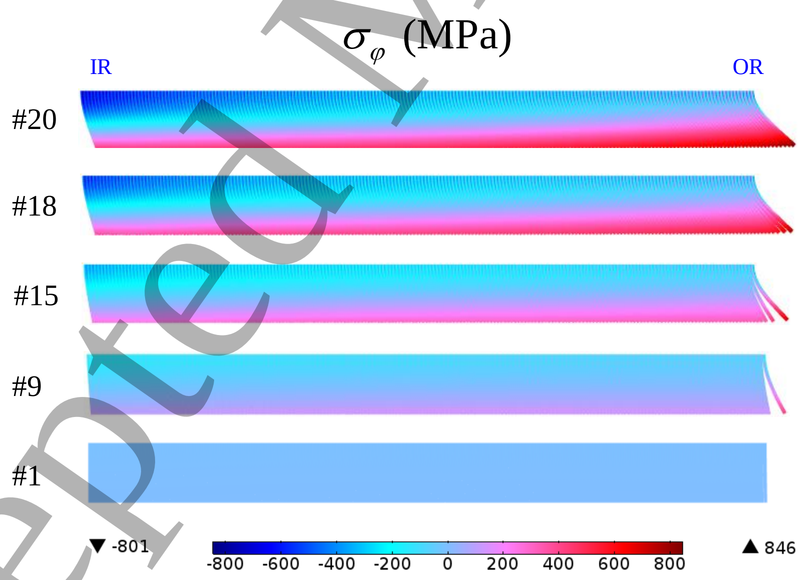

Figure 21. Hoop stress distributions in pancakes #1, #9, #15, #18, #20 at the fully-discharged moment. A deformation scale factor of 5 is used here.

Figure 21 shows the hoop stress distributions in those pancakes at the current moment. In contrast to the mechanical response at the fully-charged moment, an opposite radial shear deformation appears at the fully-discharged moment. The hoop tensile and compressive states in the upper and lower parts of the turns are reversed. This feature indicates that the cycling operation of a REBCO high field coil can cause the tape experiencing alternative positive and negative stresses and this may decrease the fatigue life of the tape and then the life of a magnet. From figure 21, it is also clear that the maximum tensile and compressive hoop stresses are located at the bottom edge of the outermost turn and the top edge of the innermost turn in a pancake, respectively. Employing an overband is supposed to be effective to restrain the movement of the outermost turn and thereby reduce the maximum tensile hoop stress in the pancake. In addition, figure 21 also shows that the stress level increases from the middle to the end of the coil winding.

Figures 22 and 23 show more detailed results for the stress and strain distributions in a pancake. Here pancake #20 is taken as a specific example and the other pancakes have consistent characteristics. From figure 22, one sees that both of the values of the hoop stress and hoop strain increase with increasing radius on different latitudes of the pancake. From figure 23, it can be seen the value of hoop strain in each turn monotonously decreases from the bottom edge to the top edge.

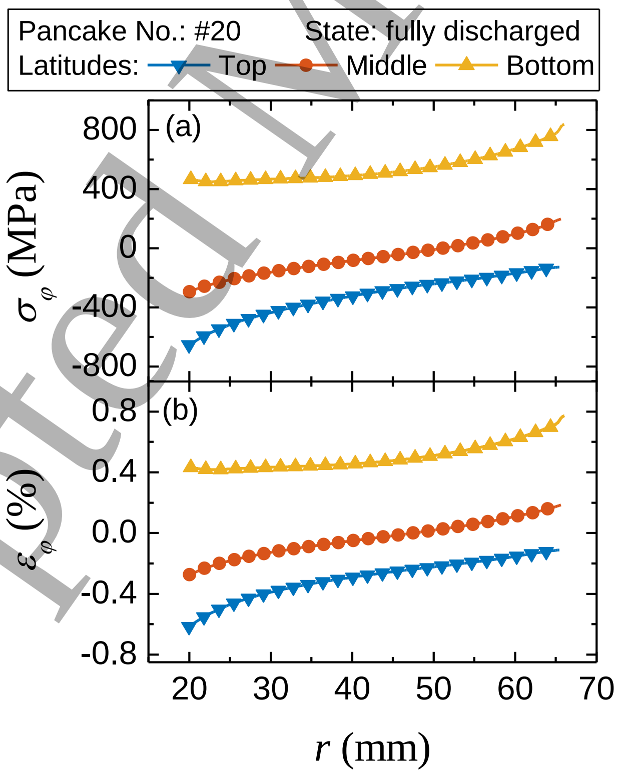

Figure 22. Profiles of (a) hoop stress and (b) hoop strain on different latitudes in pancake #20 at the fully-discharged moment.

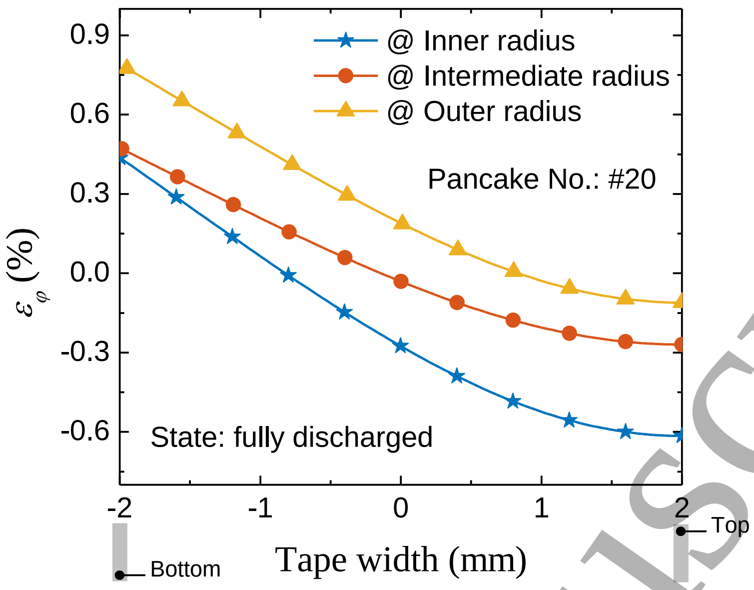

Figure 23. Hoop strain distributions in the direction of tape width at different radial positions in pancake #20 at the fully-discharged moment.

Figure 24 summarizes the maximum local hoop stresses in pancakes at the fully-discharged moment, in which the corresponding results at the fully-charged moment are redrawn for comparison. For the fully-discharged moment, it is found that the maximum local hoop stress increases with increasing pancake sequence number and the highest local hoop stress in the coil winding is located in the end pancake. The reason is that the new pair of shielding currents induced at the ramp-down stage, i.e., the pair of blue and red ones close to the top and bottom edges of the pancake shown in figure 19, penetrates into a deeper depth in the pancake with a larger sequence number, which can provide a pair of stronger driving forces for the radial shear deformation. In addition, one can see the maximum local hoop stress at the fully-discharged moment is lower than that at the fully-charged moment for a majority of pancakes in the coil winding, which is easy to understand, due to the decrease of the magnetic field at the fully-discharged moment. However, it is surprising that pancakes #18 and #20 have higher values at the fully-discharged moment. The reason is that the decrease of the magnetic field results in the turning up of the critical current and thereby a higher shielding current is induced at the fully-discharged moment (see figure 25(a)), causing the increase of the Lorentz force although the magnetic field decreases (see figure 25(b)). Consequently, the torque acting on the turn is larger.

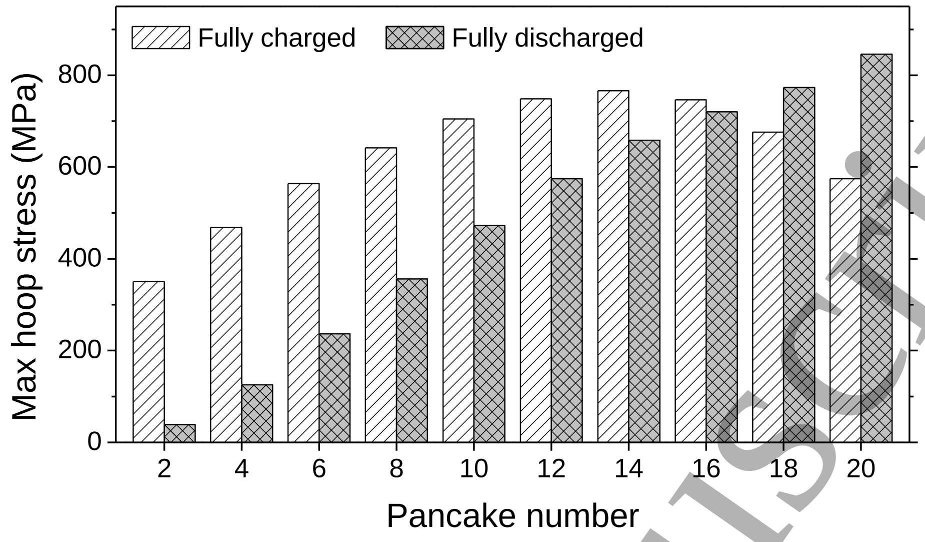

Figure 24. Comparison of the maximum local hoop stresses in pancakes between the fully-charged and fully-discharged moments.

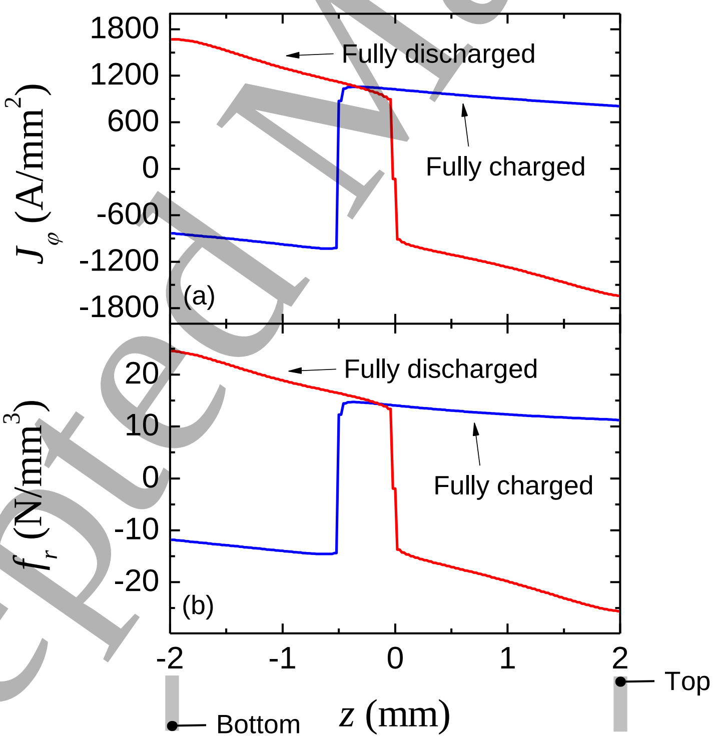

Figure 25. Profiles of (a) current density and (b) radial Lorentz force along the direction of tape width in the outermost turn of pancake #20 at the fully-charged moment and fully-discharged moment.

5. Conclusions

The mechanical responses caused by shielding current in a REBCO high field coil have been studied in this paper. Two two-dimensional axisymmetric mechanical models, i.e., the discrete contact model and the continuum bulk model, were proposed to simulate the distributions of the stress, strain and displacement in the coil winding. Moreover, both the cases with and without shielding current were simulated for comparison. Furthermore, the influences of a couple of practical factors (including the n-value, ramp rate, and operating mode of the REBCO coil winding) on the shielding current and hoop stress are studied by the discrete contact model. The conclusions are summarized as follows:

1) For the discrete contact model, nonuniform radial deformation in the direction of tape width is obtained from the case of considering the shielding current behavior; however, the radial deformation is almost uniform in the case of neglecting the shielding current behavior. The hoop stress distribution along the radial direction in the case without shielding current is consistent with that derived from the classic formula of $\sigma_{\varphi}(r) = r \cdot J_{\varphi}(r) \cdot B_z(r)$ (in which the electromagnetic field results without considering the shielding effect are used), and these results are slightly higher than the hoop stress profile on the middle latitude of the pancake in the case with shielding current. However, it is shown that the case without shielding current and the classic theoretical formula significantly underestimate the local hoop stress when compared to the case with shielding current for the hoop stresses on the top latitude of the pancake.
2) For the continuum bulk model, the nonuniform radial deformation in the direction of tape width is negligible even though the shielding current behavior is considered. The bulk model considerably underestimates the maximum local hoop stress in a majority of pancakes when compared to the discrete contact model. Moreover, the dependence of hoop stress on the radius presents a monotonously declining tendency, which is opposite to the feature in the discrete contact model. The bulk model is not adequate for the stress analysis of dry-wound high field coils, due to the prediction of unreasonably large tensile radial stress.
3) The simulations of the discrete contact model with taking shielding current into account show that for the fully-charged moment, the highest local hoop stress is located in a certain pancake near the end of the coil winding, rather than in the end

pancake; for the fully-discharged moment, it is located in the end pancake.

4) Decreasing the n-value and the ramp rate of the REBCO coil could be two auxiliary ways to suppress the shielding current and maximum local hoop stress in the coil.
5) For the ramp-and-hold mode, the shielding current and hoop stress reach the peak level at the turning-point moment and gradually decay afterwards.
6) For the ramp-up-and-down mode (noting that the background field is not ramped down with the REBCO coil), the evolution of the shielding current gives rise to a reversing of the hoop stress state in the direction of the tape width. The cycling operation of a REBCO high field coil can cause the tape experiencing alternative positive and negative stresses and this may decrease the fatigue life of the tape and then the life of a magnet. In addition, the pancakes in the vicinity of the coil end may even experience a higher hoop stress level at the fully-discharged moment in contrast to the fully-charged moment.

Appendix

Here we give the derivations of the equivalent elastic constants for the equivalent transversely isotropic homogeneous material as formulated in equation (7).

(1) $\bar{E}_1$

Considering a representative volume element (RVE) of the laminated composite co-wound tape as illustrated in figure A1, subjected to a uniaxial stretching along the 1 direction. Then, the corresponding equivalent homogeneous material satisfies a stress vs. strain relation of

$$\bar{\sigma}_1 = \bar{E}_1 \bar{\varepsilon}_1. \tag{A1}$$

The resultant force applied on an end face vertical to the 1 direction satisfies the following relation:

$$\bar{\sigma}_1 A = \sum_m \sigma_m A_m, \tag{A2}$$

where A represents the overall area of the end face, σ_m represents the tensile stress applied on the mth component material, and A_m is the corresponding area. Moreover, each component material in the RVE is regarded as an isotropic material which follows the Hooke's law, i.e.,

$$\sigma_m = E_m \bar{\varepsilon}_1. \quad \text{(A3)}$$

After substituting equations (A1) and (A3) into equation (A2), and defining $c_m = A_m / A$ as the area (or thickness) proportion for the mth component, we can get

$$\bar{E}_1 = \sum_m c_m E_m. \quad \text{(A4)}$$

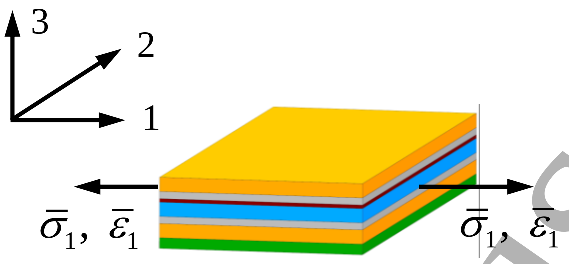

Figure A1. Schematic drawing of the RVE for the derivation of $\bar{E}_1$.

(2) $\bar{E}_3$

Considering the RVE is subjected a uniaxial stretching along the 3 direction, as shown in figure A2. Similarly, we have

$$\bar{\sigma}_3 = \bar{E}_3 \bar{\varepsilon}_3. \quad \text{(A5)}$$

The overall stretching deformation of the RVE along the 3 direction satisfies the following relation:

$$\bar{\varepsilon}_3 d = \sum_m \varepsilon_m d_m, \quad \text{(A6)}$$

where d_m and d denote the thickness of the mth component and the overall thickness of the RVE, respectively. ε_m is the tensile strain along the 3 direction in the mth component and can be calculated by the following relation once we assume every component in the RVE is subjected to an identical tensile stress of $\bar{\sigma}_3$:

$$\varepsilon_m = \frac{\bar{\sigma}_3}{E_m}. \quad \text{(A7)}$$

Substituting equations (A5) and (A7) into equation (A6) and considering $d_m / d = A_m / A = c_m$, one can get

$$\frac{1}{\bar{E}_3} = \sum_m \frac{c_m}{E_m}. \quad \text{(A8)}$$

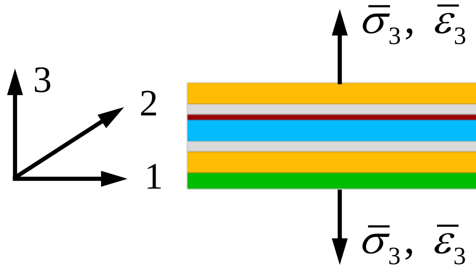

Figure A2. Schematic drawing of the RVE for the derivation of $\bar{E}_3$.

(3) $\bar{\nu}_{21}$

Considering the RVE is subjected to a uniaxial stretching along the 1 direction, which leads to a contraction deformation along the 2 direction as shown in figure A3. The macroscopic strain components $\bar{\varepsilon}_1$ and $\bar{\varepsilon}_2$ satisfy the definition of

$$\bar{\varepsilon}_2 = -\bar{\nu}_{12}\bar{\varepsilon}_1. \tag{A9}$$

In order to guarantee every component in the RVE has an identical contraction strain of $\bar{\varepsilon}_2$ in the 2 direction, internal stresses must be yielded in the components along that direction. The RVE should satisfy an internal force equilibrium in the 2 direction, i.e.,

$$\sum_m c_m \sigma_m^{\text{int}} = 0. \tag{A10}$$

Based on the superposition theory of linear elastic mechanics, the 2-direction strain in each component can be decomposed into the contraction strain attributed to the uniaxial stretching along the 1 direction and the internal strain attributed to the internal stress. Therefore, we have

$$\bar{\varepsilon}_2 = -\nu_m \bar{\varepsilon}_1 + \frac{\sigma_m^{\text{int}}}{E_m}. \tag{A11}$$

Substituting equations (A9) and (A11) into equation (A10), one can get

$$\bar{\nu}_{12} = \frac{\sum_m c_m \nu_m E_m}{\sum_m c_m E_m}. \tag{A12}$$

Considering the relation of $\bar{\nu}_{ij} / \bar{E}_i = \bar{\nu}_{ji} / \bar{E}_j$ originating from the symmetrical property of the elastic compliance matrix and $\bar{E}_1 = \bar{E}_2$, we have

$$\bar{\nu}_{21} = \bar{\nu}_{12} = \frac{\sum_m c_m \nu_m E_m}{\sum_m c_m E_m}. \tag{A13}$$

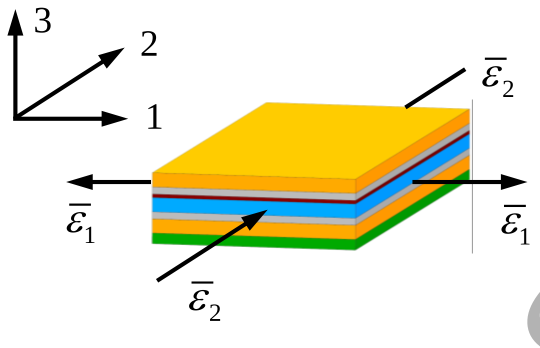

Figure A3. Schematic drawing of the RVE for the derivation of $\bar{\nu}_{21}$.

(4) $\bar{\nu}_{31}$

Considering the RVE is subjected a uniaxial stretching along the 1 direction, as shown in figure A4. The macroscopic strain components $\bar{\varepsilon}_1$ and $\bar{\varepsilon}_3$ satisfy the definition of

$$\bar{\varepsilon}_3 = -\bar{\nu}_{13}\bar{\varepsilon}_1. \tag{A14}$$

The overall contraction deformation of the RVE along the 3 direction satisfies the following relation:

$$\bar{\varepsilon}_3 d = \sum_m \varepsilon_m d_m, \tag{A15}$$

in which the 3-direction strain ε_m in each component can be calculated by

$$\varepsilon_m = -\nu_m \bar{\varepsilon}_1. \tag{A16}$$

Substituting equations (A14) and (A16) into equation (A15), one can get

$$\bar{\nu}_{13} = \sum_m c_m \nu_m. \tag{A17}$$

Again considering the relation of $\bar{\nu}_{ij} / \bar{E}_i = \bar{\nu}_{ji} / \bar{E}_j$, we can get

$$\bar{\nu}_{31} = \frac{\bar{E}_3}{\bar{E}_1}\bar{\nu}_{13} = \frac{\bar{E}_3}{\bar{E}_1}\sum_m c_m \nu_m. \tag{A18}$$

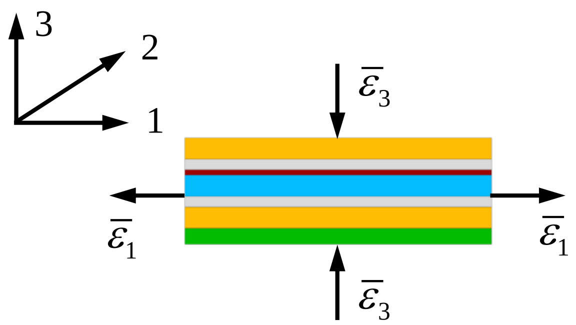

Figure A4. Schematic drawing of the RVE for the derivation of $\bar{\nu}_{31}$.

(5) $\bar{G}_{23}$

Considering the RVE experiences a shear deformation in the 2-3 plane, as shown in figure A5. The macroscopic stress $\bar{\tau}_{23}$ and macroscopic strain $\bar{\gamma}_{23}$ follow the Hooke's law in shear, i.e.,

$$\bar{\tau}_{23} = \bar{G}_{23}\bar{\gamma}_{23}. \tag{A19}$$

The overall shear deformation of the RVE satisfies the following relation:

$$\bar{\gamma}_{23}d = \sum_m \gamma_m d_m, \tag{A20}$$

where the shearing strain in each component γ_m can be calculated by the following relation once we assume every component in the RVE is subjected to an identical shearing stress of $\bar{\tau}_{23}$:

$$\gamma_m = \frac{\bar{\tau}_{23}}{G_m}. \tag{A21}$$

Substituting equations (A19) and (A21) into equation (A20), one can get

$$\frac{1}{\bar{G}_{23}} = \sum_m \frac{c_m}{G_m}. \tag{A22}$$

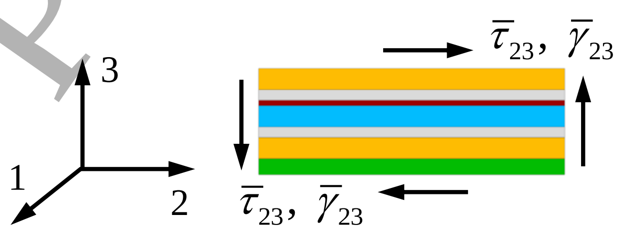

Figure A5. Schematic drawing of the RVE for the derivation of $\bar{G}_{23}$.

Acknowledgments

This work was supported in part by the National Natural Science Foundation of China under Grant Nos. 11802036 and 11872195. This work was also partially performed at the National High Magnetic Field Laboratory, which was supported by the U.S. National Science Foundation Cooperative Agreement No. DMR-1644779 and the State of Florida. We thank the colleagues who participated in the discussions on the shielding current and high stress issues in the activities of developing and constructing the NHMFL 32 T all-superconducting magnet.

References

[1] Mitchell N 2002 Analysis of the effect of Nb_3Sn strand bending on CICC superconductor performance *Cryogenics* **42** 311-25

[2] Nijhuis A, Ilyin Y, Abbas W, Ten Haken B and Ten Kate H H J 2004 Performance of an ITER CS1 model coil conductor under transverse cyclic loading up to 40,000 cycles *IEEE Trans. Appl. Supercond.* **14** 1489-94

[3] Nijhuis A 2008 A solution for transverse load degradation in ITER Nb_3Sn CICCs: verification of cabling effect on Lorentz force response *Supercond. Sci. Technol.* **21** 054011

[4] Zhai Y and Bird M D 2008 Florida electro-mechanical cable model of Nb_3Sn CICCs for high-field magnet design *Supercond. Sci. Technol.* **21** 115010

[5] Bajas H, Durville D, Ciazynski D and Devred A 2010 Numerical simulation of the mechanical behavior of ITER cable-in-conduit conductors *IEEE Trans. Appl. Supercond.* **20** 1467-70

[6] Iwasa Y 2009 Case studies in superconducting magnets (2nd ed) *New York: Springer-Verlag*

[7] https://nationalmaglab.org/

[8] Kajita K, Iguchi S, Xu Y, Nawa M, Hamada M, Takao T, Nakagome H, Matsumoto S, Nishijima G, Suematsu H, Takahashi M and Yanagisawa Y 2016 Degradation of a REBCO coil due to cleavage and peeling originating from an electromagnetic force *IEEE Trans. Appl. Supercond.* **26** 4301106

[9] Wilson M N 1983 Superconducting Magnets *Oxford: Clarendon*

[10] Gray W H and Ballou J K 1977 Electromechanical stress analysis of transversely isotropic solenoids *J. Appl. Phys.* **48** 3100-9

[11] Park M J, Kwak S Y, Kim W S, Lee S W, Hahn S Y, Lee J K, Han J H, Choi K D, Jung H K, Seong K C and Hahn S Y 2007 Stress analysis of HTS magnet for a 600 kJ SMES *IEEE Trans. Appl. Supercond.* **17** 1994-7

[12] Choi S, Kiyoshi T, Hahn S and Sugano M 2009 Stress analysis of a high temperature superconductor coil wound with Bi-2223/Ag tapes for high field HTS/LTS NMR magnet application *IEEE Trans. Appl. Supercond.* **19** 2237-40

[13] Kim Y, Hahn S, Voccio J, Song J, Bascuñán J and Iwasa Y 2015 Strain in YBCO double-pancake coil with stainless steel overband under external magnetic field *IEEE Trans. Appl. Supercond.* **25** 4300504

[14] Liu D, Zhang W, Yong H and Zhou Y 2018 Thermal stability and mechanical behavior in no-insulation high-temperature superconducting pancake coils *Supercond. Sci. Technol.* **31** 085010

[15] Wang L, Wang Q, Li L, Qin L, Liu J, Li Y and Hu X 2018 The effect of winding conditions on the stress distribution in a 10.7 T REBCO insert for the 25.7 T superconducting magnet *IEEE Trans. Appl. Supercond.* **28** 4600805

[16] Wang L, Wang Q, Li L, Qin L, Liu J, Hu X and Li Y 2018 Stress analysis of winding process, cooling down, and excitation in a 10.7 T REBCO HTS magnet *IEEE Trans. Appl. Supercond.* **28** 4603305

[17] Liu D, Zhang W, Yong H and Zhou Y 2019 Numerical analysis of thermal stability and mechanical response in a no-insulation high-temperature superconducting layer-wound coil *Supercond. Sci. Technol.* **32** 044001

[18] Xia J, Bai H, Lu J, Gavrilin A V, Zhou Y and Weijers H W 2015 Electromagnetic modeling of REBCO high field coils by the H-formulation *Supercond. Sci. Technol.* **28** 125004

[19] Pardo E, Šouc J and Frolek L 2015 Electromagnetic modelling of superconductors with a smooth current-voltage relation: variational principle and coils from a few turns to large magnets *Supercond. Sci. Technol.* **28** 044003

[20] Berrospe-Juarez E, Zermeño V M R, Trillaud F, Gavrilin A V, Grilli F, Abraimov D V, Hilton D K and Weijers H W 2018 Estimation of losses in the (RE)BCO two-coil insert of the NHMFL 32 T all-superconducting magnet *IEEE Trans. Appl. Supercond.* **28** 4602005

[21] Weijers H W, Markiewicz W D, Voran A J, Gundlach S R, Sheppard W R, Jarvis B J, Johnson Z L, Noyes P D, Lu J, Kandel H, Bai H, Gavrilin A V,

Viouchkov Y L, Larbalestier D C and Abraimov D V 2014 Progress in the development of a superconducting 32 T magnet with REBCO high field coils *IEEE Trans. Appl. Supercond.* **24** 4301805

[22] Weijers H W, Markiewicz W D, Gavrilin A V, Voran A J, Viouchkov Y L, Gundlach S R, Noyes P D, Abraimov D V, Bai H, Hannahs S T and Murphy T P 2016 Progress in the development and construction of a 32-T superconducting magnet *IEEE Trans. Appl. Supercond.* **26** 4300807

[23] Hilton D K, Gavrilin A V and Trociewitz U P 2015 Practical fit functions for transport critical current versus field magnitude and angle data from (RE)BCO coated conductors at fixed low temperatures and in high magnetic fields *Supercond. Sci. Technol.* **28** 074002

[24] Hong Z and Coombs T A 2010 Numerical modelling of AC loss in coated conductors by finite element software using *H* formulation *J. Supercond. Nov. Magn.* **23** 1551-62

[25] Rodriguez-Zermeno V M, Mijatovic N, Træholt C, Zirngibl T, Seiler E, Abrahamsen A B, Pedersen N F and Sørensen M P 2011 Towards faster FEM simulation of thin film superconductors: a multiscale approach *IEEE Trans. Appl. Supercond.* **21** 3273-6

[26] Zermeno V M R, Abrahamsen A B, Mijatovic N, Jensen B B and Sørensen M P 2013 Calculation of alternating current losses in stacks and coils made of second generation high temperature superconducting tapes for large scale applications *J. Appl. Phys.* **114** 173901

[27] Brambilla R, Grilli F and Martini L 2007 Development of an edge-element model for AC loss computation of high-temperature superconductors *Supercond. Sci. Technol.* **20** 16-24

[28] https://www.comsol.com/

[29] Clickner C C, Ekin J W, Cheggour N, Thieme C L H, Qiao Y, Xie Y Y and Goyal A 2006 Mechanical properties of pure Ni and Ni-alloy substrate materials for Y–Ba–Cu–O coated superconductors *Cryogenics* **46** 432-8

[30] Roa J J, Capdevila X G, Martínez M, Espiell F and Segarra M 2007 Nanohardness and Young's modulus of YBCO samples textured by the Bridgman technique *Nanotechnology* **18** 385701

[31] Ravinder Reddy R, Murakami M, Tanaka S and Venugopal Reddy P 1996 Elastic behavior of a Y-Ba-Cu-O sample prepared by the MPMG method

Physica C **257** 137-42

[32] COMSOL Multiphysics material library

[33] Zhang Y, Hazelton D W, Kelley R, Kasahara M, Nakasaki R, Sakamoto H and Polyanskii A 2016 Stress–strain relationship, critical strain (stress) and irreversible strain (stress) of IBAD-MOCVD-based 2G HTS wires under uniaxial tension *IEEE Trans. Appl. Supercond.* **26** 8400406

[34] COMSOL structural mechanics module user's guide (version: 5.2)

[35] van der Laan D C, Ekin J W, Clickner C C and Stauffer T C 2007 Delamination strength of YBCO coated conductors under transverse tensile stress *Supercond. Sci. Technol.* **20** 765-70

[36] Kajita K, Takao T, Maeda H and Yanagisawa Y 2017 Degradation of a REBCO conductor due to an axial tensile stress under edgewise bending: a major stress mode of deterioration in a high field REBCO coil's performance *Supercond. Sci. Technol.* **30** 074002

[37] Yanagisawa Y, Nakagome H, Uglietti D, Kiyoshi T, Hu R, Takematsu T, Takao T, Takahashi M and Maeda H 2010 Effect of YBCO-coil shape on the screening current-induced magnetic field intensity *IEEE Trans. Appl. Supercond.* **20** 744-7

[38] Zhang M, Yuan W, Hilton D K, Dalban-Canassy M and Trociewitz U P 2014 Study of second-generation high-temperature superconducting magnets: the self-field screening effect *Supercond. Sci. Technol.* **27** 095010